Supplementary Information for

Assembling a single active pocket by enzyme and metal modules for simultaneously catalyzing oxidation-reduction cascades

Yunkai Fan[1], Jia Hu[1], Qilu Wu[2], Mengyu Zhu[2], Haozhi Wang[4], Jun Ge[2, 3*], Xiaoyang Li[1*]

1 State Key Laboratory of Food Science and Technology, School of Food Science and Technology, Nanchang University, Nanchang 330047, China.

2 Key Lab for Industrial Biocatalysis, Ministry of Education, Department of Chemical Engineering, Tsinghua University, Beijing 100084, China.

3 State Key Laboratory of Green Biomanufacturing, Beijing 100084, China

4 State Key Laboratory of Marine Resource Utilization in South China Sea, School of Materials Science and Engineering, Hainan University, Haikou 300350, China.

Email: junge@mail.tsinghua.edu.cn; xyli@ncu.edu.cn

Supplementary Materials and Methods

Chemicals:

Palladium (II) acetate ($Pd(OAc)_2$, 48 wt.%), chloroplatinic acid hydrate ($H_2PtCl_6 \cdot xH_2O$，99.995 wt.%), zirconyl chloride octahydrate ($ZrOCl_2.8H_2O$, 99 wt.%), tetra(4-carboxyphenyl)porphyrin (TCPP, ≥98%), deuterium oxide (D_2O, ≥99.9%), 2,2’-azino-bis(3-ethylbenzthiazoline-6-sulfonic acid) (ABTS, ≥98%), 3,3’,5,5’-tetramethylbenzidine (TMB, ≥98%), laccase (from *Aspergillus*) were purchased from Sigma. N,N-dimethylformamide (DMF, AR, ≥99.5%) was purchased from Aladdin. Aflatoxin B_1 (AFB_1, ≥98%), ochratoxin A (OTA, ≥98%), zearalenone (ZEN, ≥98%), deoxynivalenol (DON, ≥98%), T-2 toxin (T-2, ≥98%) were purchased from Pribolab (China). HPLC-grade methanol and acetonitrile were purchased from Tedia Company Inc. (Ohio, USA) and used after filtration through a 0.22 µm organic membrane. Deionized water was purified and prepared using an in-house Milli-Q Ultrapure water system (Millipore, Milford, MA, USA).

Characterization:

The X-ray absorption data at the Pd K-edge of PCN(PtPd) and Pd foil, along with the Pt L-edge of PCN(PtPd) and Pt foil, were collected at the X-ray absorption fine structure (XAFS) station of the Shanghai Synchrotron Radiation Facility (SSRF), China. Data analysis was performed using the software Athena. The EXAFS data fitting was performed in the Artemis program.

For Cryo-ET imaging of PCN(PtPd)-Lac or PCN(PtPd), a 6-μL aliquot containing a 1:1 mixture of sample solution: gold fiducial beads (10 nm diameter, Aurion, The Netherlands) was applied onto a glow discharged copper grid coated with holey carbon (C-flat; Protochips, Raleigh, NC) prior to plunge-freezing. The grids were single-side blotted away from the sample side for 3.5 s, vitrified by plunge-freezing into liquid ethane using a Vitrobot Mark IV (Thermal Fisher Scientific). The grids were screened using a Tecnai Arctica microscope operated at a voltage of 200 kV equipped with a Falcon III direct electron detector (Thermal Fisher Scientific). Grids with continuous carbon and thin ice were subsequently imaged on a Titan Krios microscope operated at a voltage of 300 kV equipped with an energy filter (slit width 20 eV; GIF Quantum LS, Gatan) and K2 Summit direct electron detector (Gatan). For tilt-series data collection, the stage was tilted from -60° to 60° at 3° step. The electron beam induced motion was corrected by MotionCor[1]by averaging 8 frames for each tilt. Defocus of the tilt series were measured using CTFFIND4[2]. The tilt series were contrast transfer function corrected and tomograms were reconstructed by weighted back projection in IMOD[3] . Four times binned tomograms were intensity inverted and visualized in UCSF Chimera[4] .

The Pt and Pd contents of PCN(PtPd) and PCN(PtPd)-Lac were determined using inductively coupled plasma optical emission spectroscopy (ICP-OES, Agilent 5110, Agilent Technologies, USA).

Transmission electron microscopy (TEM), high-resolution TEM (HRTEM) and energy dispersive X-ray (EDX) were conducted on a JEOL JEM-2100F instrument working at 120 kV.

High-angle annular dark-field scanning transmission electron microscopy (HAADF-STEM) and EDS mapping were recorded on a JEOL JEM-2100F instrument operated at 200 kV.

AC-STEM images were acquired using a FEI Titan G2 60-300 transmission electron microscopy operated at an acceleration voltage of 300 kV.

Scanning electron microscope (SEM) images of samples were taken on a JSM 7401 field emission gun-scanning electron microscope at an accelerating voltage of 3.0-10.0 kV. The lyophilized powder of samples was firstly attached to a carbon paste and then sputter-coated with a thin layer of conductive gold to improve the electrical conductivity.

The activities of enzyme catalysts were determined on a UV/Vis spectrophotometer HITACHI U-3900.

Photocurrent and Mott-Schottky measurements of PCN, PCN(Pt), PCN(Pd), PCN(PtPd), and PCN(PtPd)-Lac were performed on a CHI760E electrochemical workstation (CH Instruments, China). A three-electrode configuration was used, with the sample as the working electrode, a platinum wire as the counter electrode, and an Ag/AgCl electrode as the reference. Photocurrent tests were conducted under simulated sunlight (AM 1.5G, 100 mW/cm^2), while Mott-Schottky measurements were performed in 0.1 M Na_2SO_4 at 1 kHz over a potential range of -0.6 to 0.6 V.

Electron spin resonance (ESR) spectroscopy measurements for Lac, PCN(PtPd), and PCN(PtPd)-Lac were performed on a Bruker EMXplus-6/1 spectrometer (Bruker, Germany).

The UV/Vis diffuse reflectance spectra (UV/Vis DRS) of PCN, PCN(Pt), PCN(Pd), PCN(PtPd), and PCN(PtPd)-Lac were recorded using a Shimadzu UV-3600i Plus spectrophotometer (Shimadzu, Japan).

Thermogravimetric analysis (TGA) of Lac, PCN(PtPd), and PCN(PtPd)-Lac were conducted using a Netzsch STA 449 F5 thermogravimetric analyzer (Netzsch, Germany).

The Brunauer–Emmett–Teller (BET) specific surface area and pore size distribution of PCN(PtPd) and PCN(PtPd)-Lac were measured using a Micromeritics ASAP 2460 surface area and porosity analyzer (Micromeritics, USA).

The photocatalytic experiments were conducted using a multi-channel photocatalytic reaction system (PCX50C). The system provides adjustable power ranging from 1 to 5 W and is equipped with 9 reaction positions.

Laccase was fluorescently labeled with fluorescein isothiocyanate (FITC) before the characterization of CLSM. The laccase solution (1.5 mL, 10 mg/mL in PBS at pH 7.5) was mixed with the FITC solution (50 μL, 20 mg/mL in DMSO). The mixture was then reacted overnight at 4°C. After the reaction, the mixture was dialyzed against PBS for 72 hours to remove the unbound fluorescent dye.

Preparation of PCN(Pt) and PCN(Pd)

The single-atom catalyst PCN(Pt) was synthesized using a hydrothermal method. PCN-224 (10 mg) was dispersed in DMF (4 mL). 200 μL of H_2PtCl_6 aqueous solution (100 mg /mL) was added under magnetic stirring. The mixture was sonicated at 25 ^oC for 10 min, and then transferred to a 20 mL stainless-steel autoclave and heated at 80^oC for 4 h. Then, PCN(Pt) was collected by centrifugation at 10000 rpm for 5 minutes and washed by water for three times. PCN(Pd) was prepared using the same method by replacing H_2PtCl_6 with $Pd(OAc)_2$.

Supplementary Figures

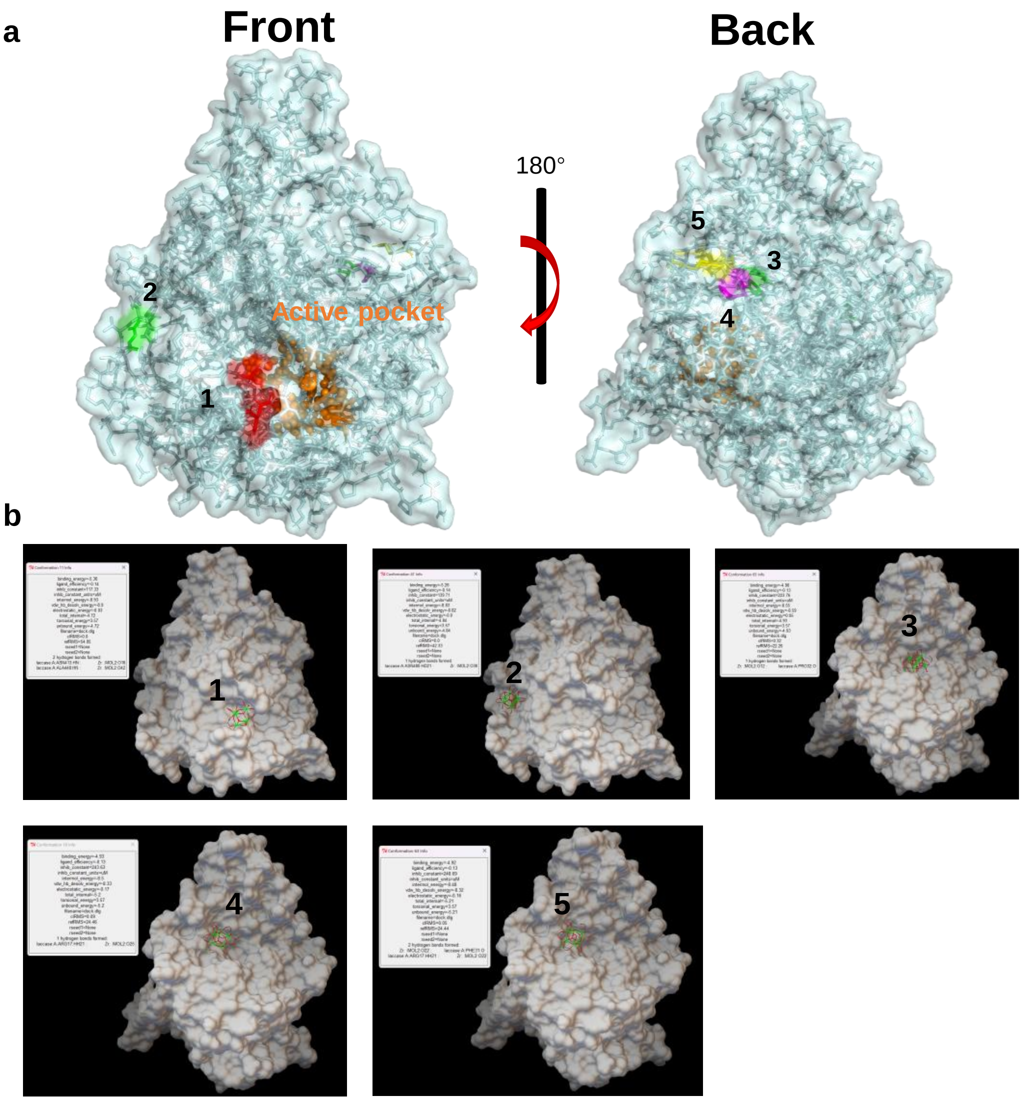

c

Position	Amino acid residues	Binding energy (Kcal/mol)
1	ASN413、ALA448	-5.36
2	ASN480	-5.26
3	PRO32	-4.98
4	ARG17	-4.93
5	PHE31、ARG17	-4.92

Supplementary Figure 1. (a) Five most possible binding sites of the $Zr_6O_4(OH)_4$ clusters of PCN-224 with laccase (front and back views) calculated by Molecular docking. Orange: active site of laccase. **(b)** Raw docking results visualized in AutoDock software. **(c)** Amino acid residues and the corresponding binding energies involved in coordination with $Zr_6O_4(OH)_4$ clusters.

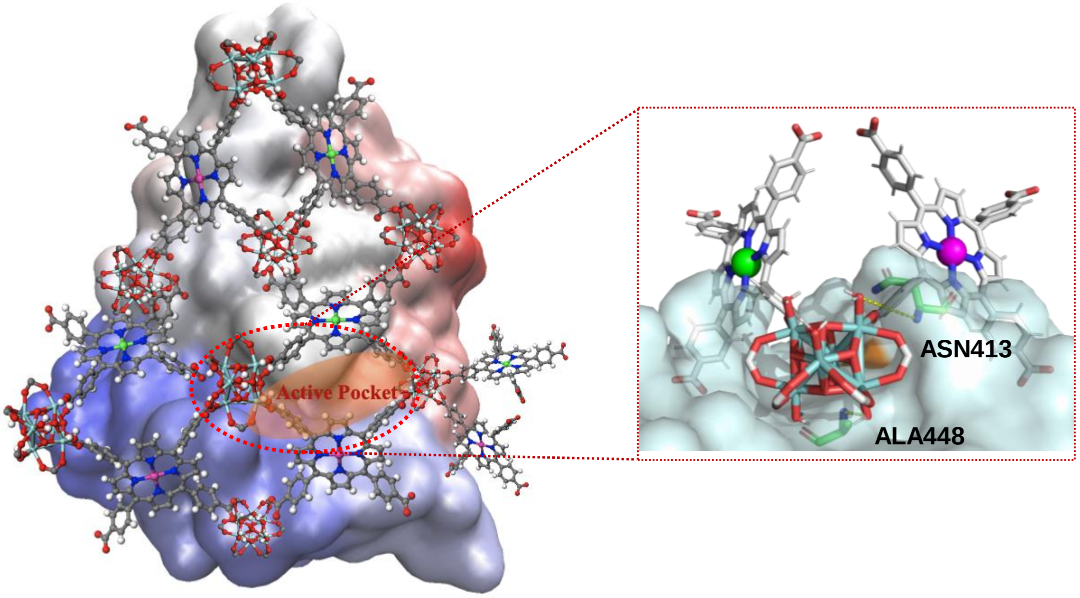

Supplementary Figure 2. Overview of PCN(PtPd)-Lac. The magnified configuration shows the structure of $Zr_6O_4(OH)_4$ cluster binding with the active center-adjacent amino acids of laccase (Asn413 and Ala448).

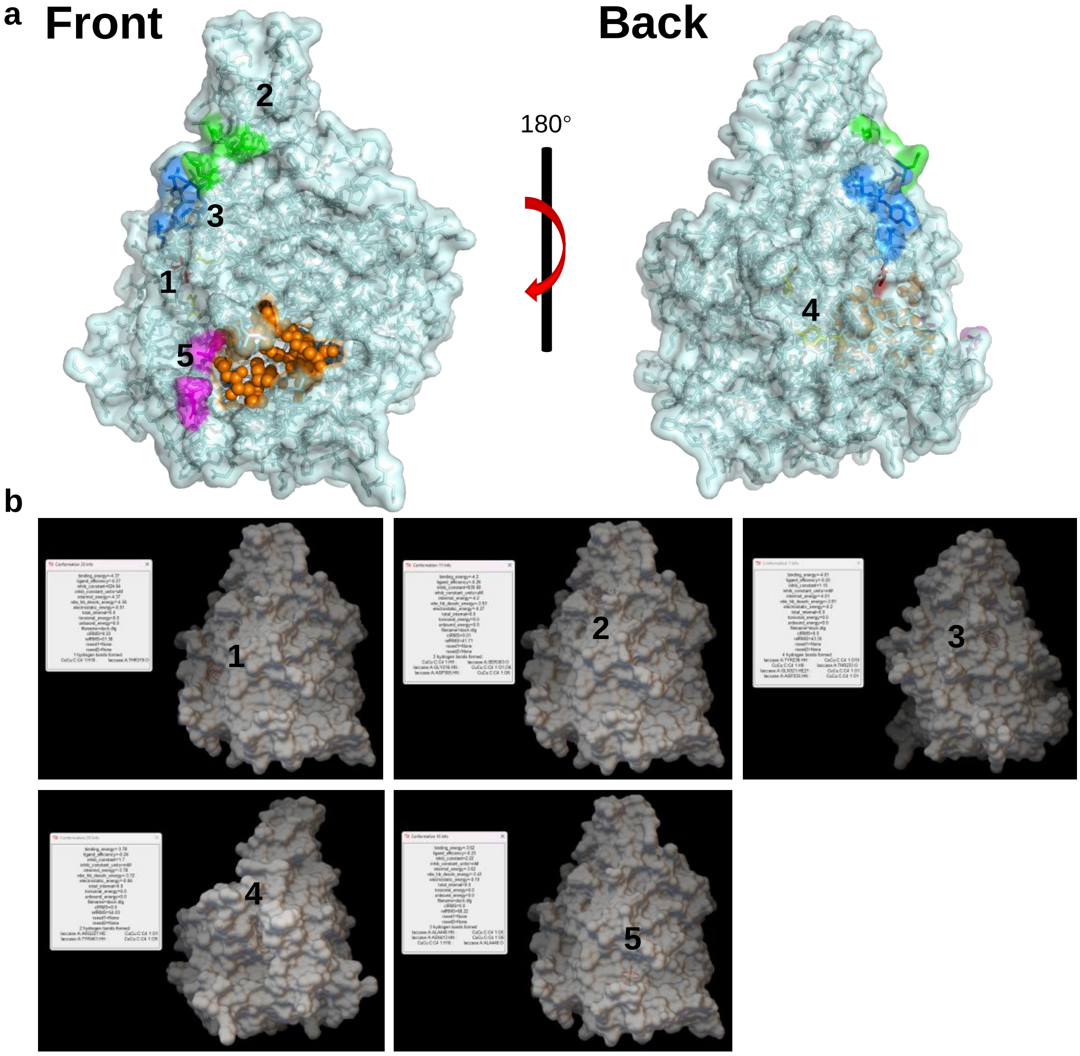

c

Position	Amino acid residues	Binding energy (Kcal/mol)
1	THR319	-4.37
2	SER303、GLY216、ASP305	-4.2
3	TYR236、TYR233、GLN321、ASP235	-4.01
4	ARG227、TYR461	-3.78
5	ALA448、ASN413、	-3.62

Supplementary Figure 3. (a) Five most possible binding sites of the $Cu_2(CO_2)_4$ clusters of HKUST-1 with laccase (front and back views) calculated by Molecular docking. Orange: active site of laccase. **(b)** Raw docking results visualized in AutoDock software. **(c)** Amino acid residues and the corresponding binding energies involved in coordination with $Cu_2(CO_2)_4$ clusters.

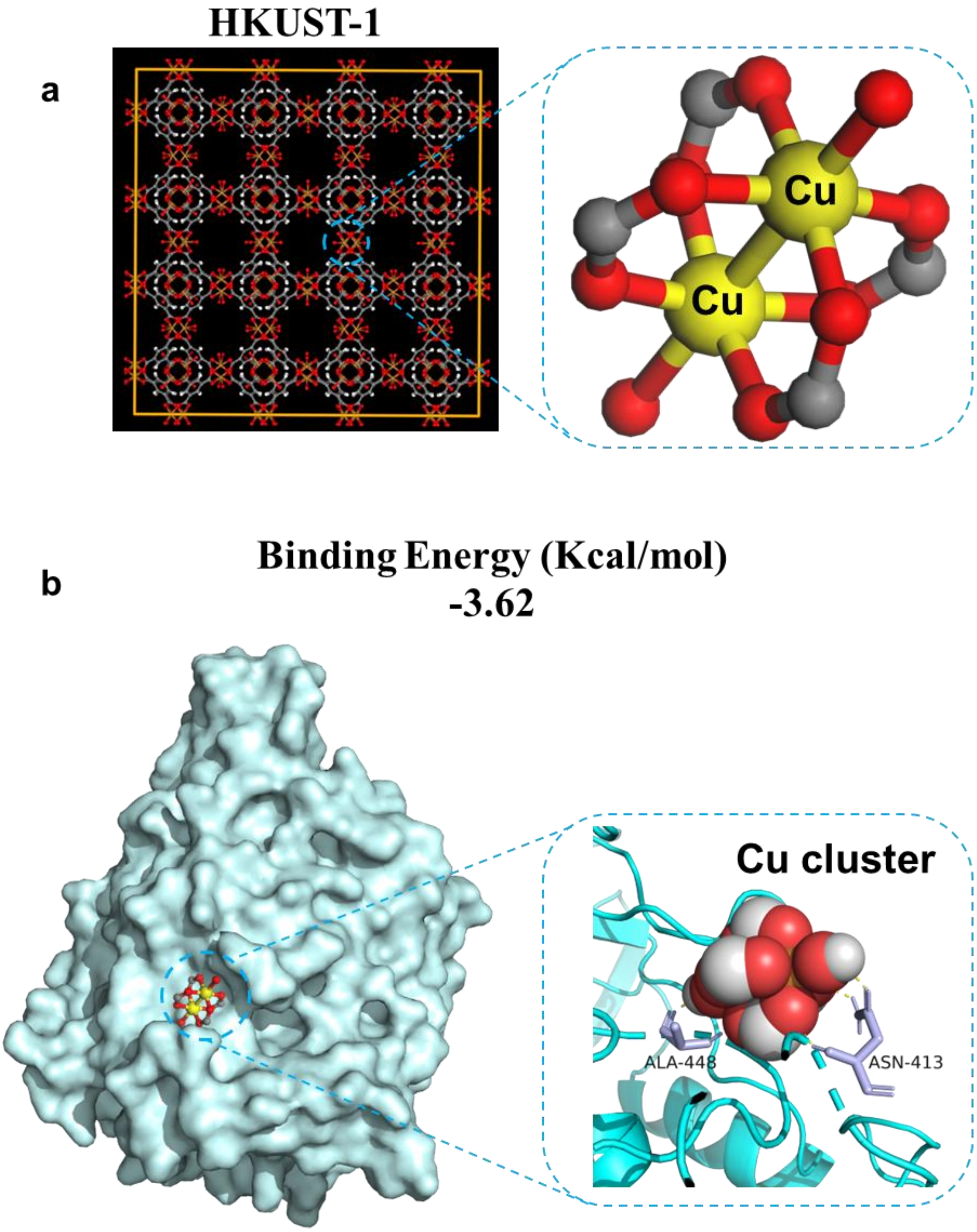

Supplementary Figure 4. (a) Molecular model of the $Cu_2(CO_2)_4$ binuclear copper cluster of HKUST-1. (b) The overall structure of the Cu cluster binding to laccase near the active site and the corresponding binding energy.

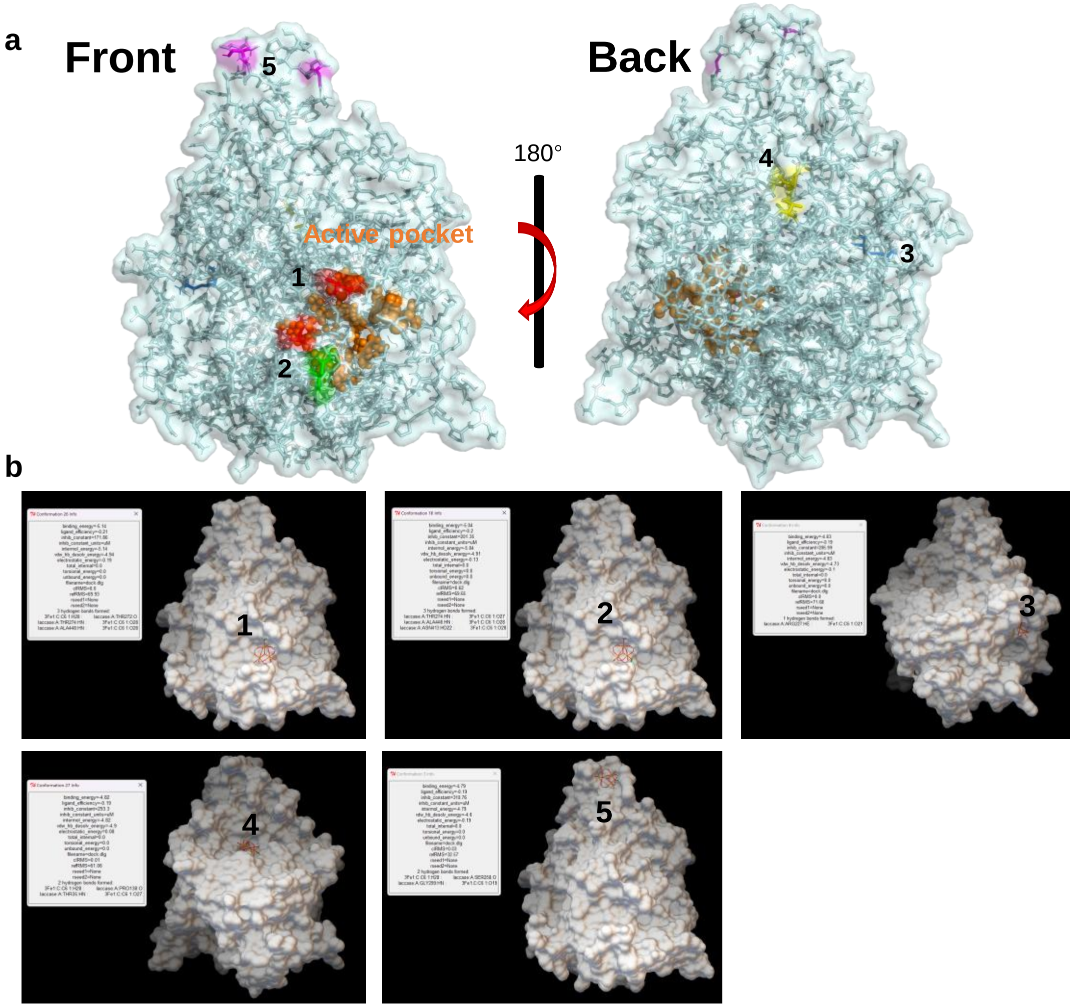

c

Position	Amino acid residues	Binding energy (Kcal/mol)
1	THR274、ALA448	-5.14
2	THR274、ALA448、ASN413	-5.04
3	ARG227	-4.83
4	PRO138、THR35	-4.82
5	SER258、GLY299	-4.79

Supplementary Figure 5. (a) Five most possible binding sites of the $Fe_3O(CO_2)_6$ clusters of MIL-100(Fe) with laccase (front and back views) calculated by Molecular docking. Orange: active site of laccase. **(b)** Raw docking results visualized in AutoDock software. **(c)** Amino acid residues and the corresponding binding energies involved in coordination with $Fe_3O(CO_2)_6$ clusters.

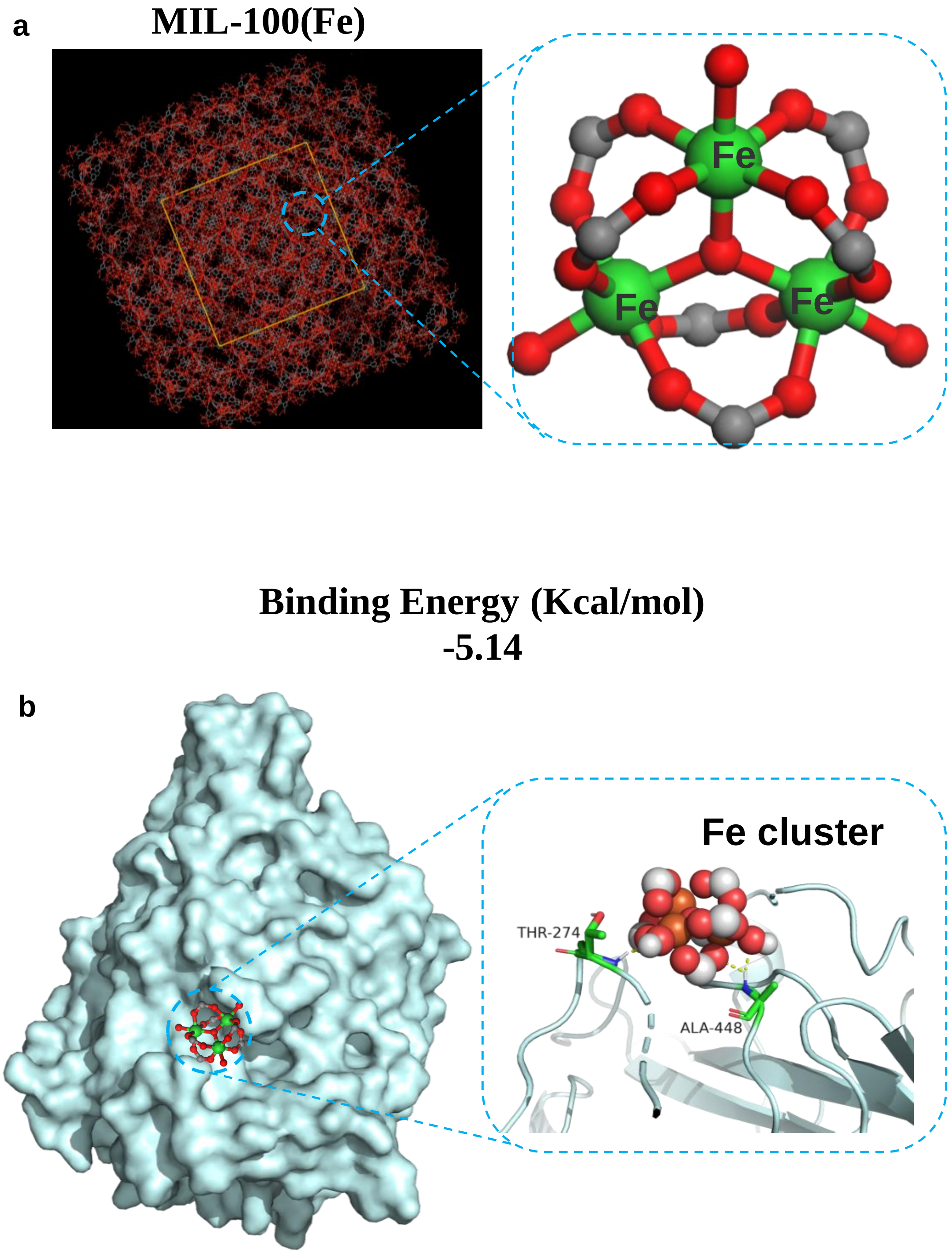

Supplementary Figure 6. (a) Molecular model of the $Fe_3O(CO_2)_6$ trinuclear iron cluster of MIL-100(Fe). (b) The overall structure of the Fe cluster binding to laccase near the active site and the corresponding binding energy.

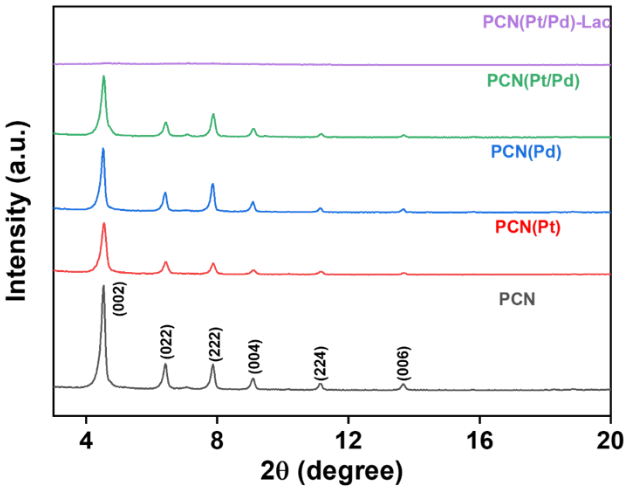

Supplementary Figure 7. XRD patterns of PCN-224, PCN(Pt), PCN(Pd), PCN(PtPd), and PCN(PtPd)-Lac. The diffraction peaks correspond to the characteristic planes of the crystalline structures.

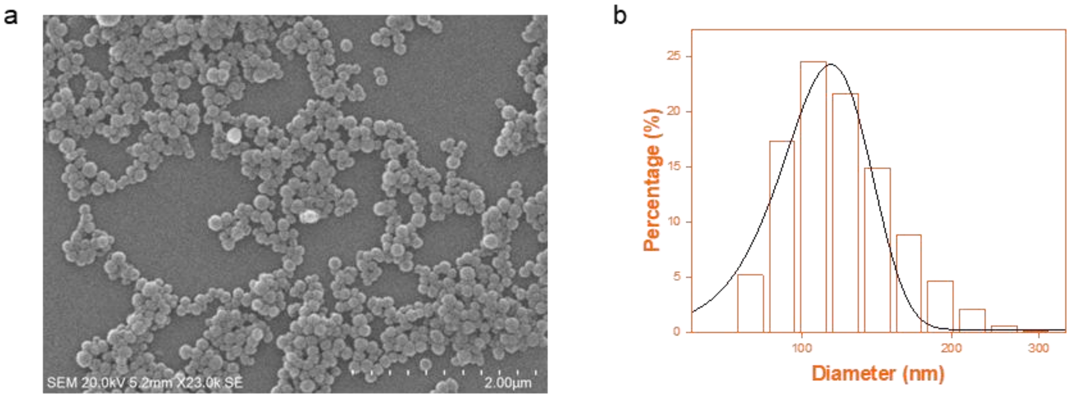

Supplementary Figure 8. SEM images of PCN-224 and the corresponding particle size distribution calculated using software Nano Measurer 1.2.

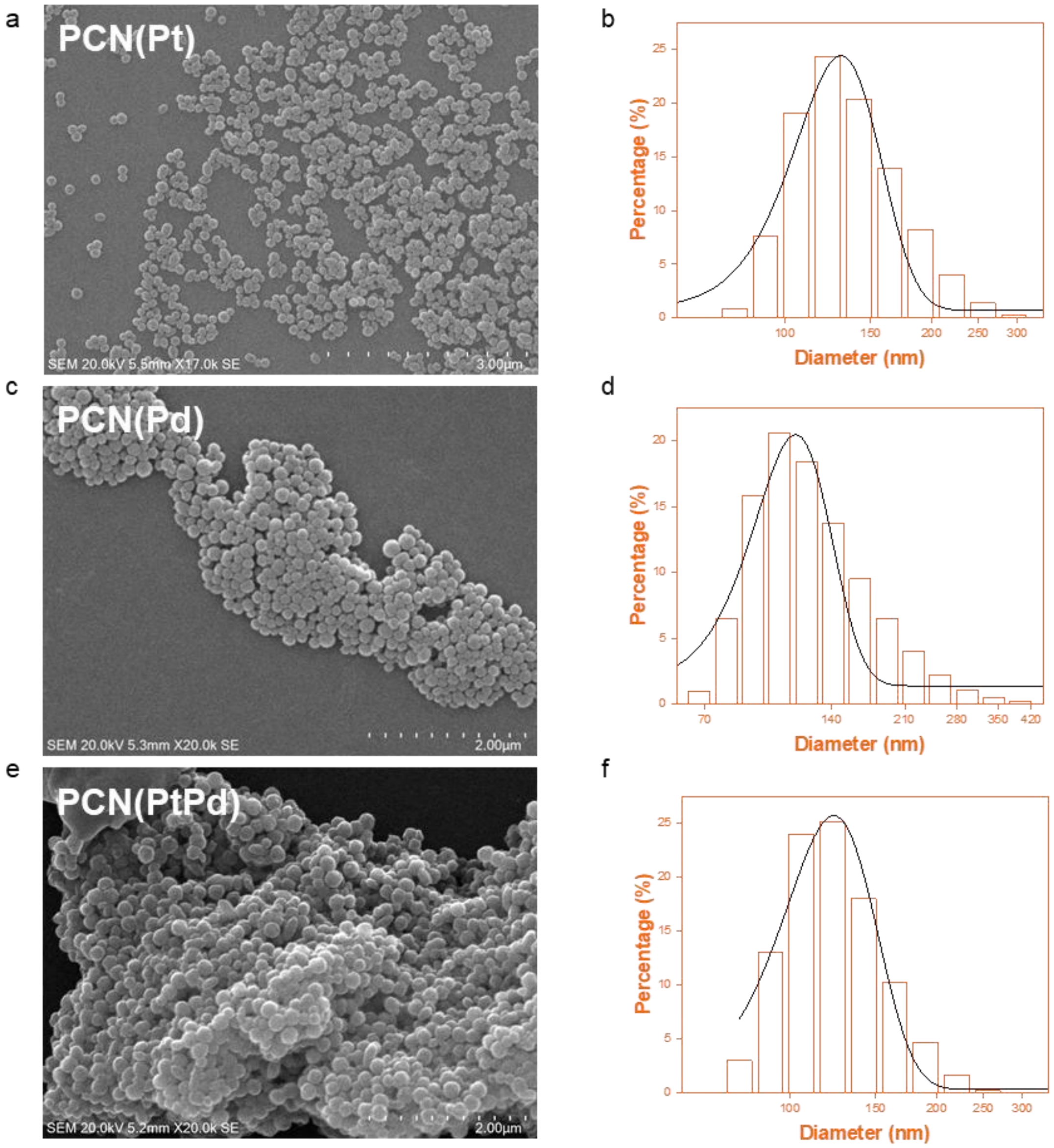

Supplementary Figure 9. SEM images of PCN(Pt), PCN(Pd), and PCN(PtPd) and the corresponding particle size distribution calculated using software Nano Measurer 1.2.

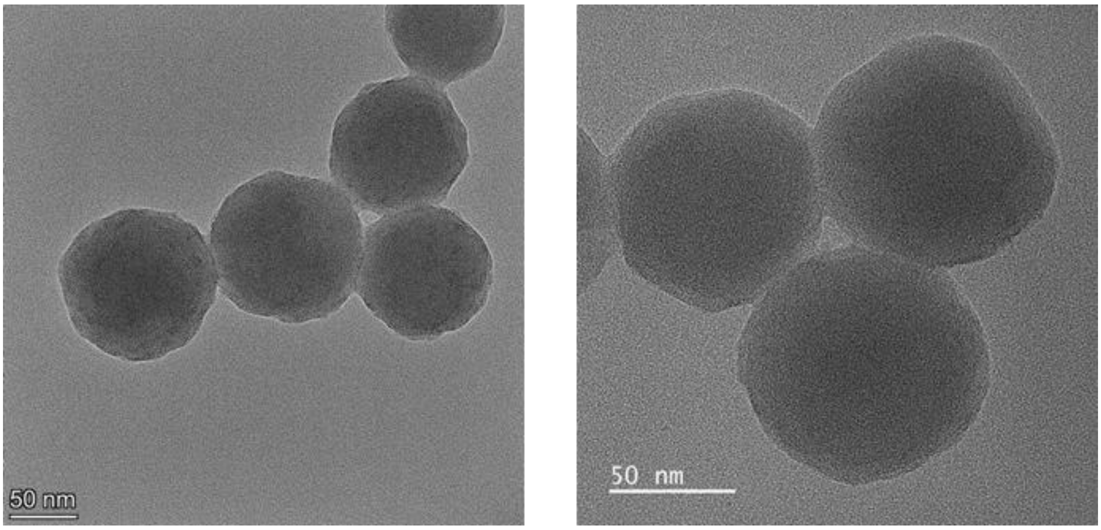

Supplementary Figure 10. Representative TEM images of PCN(PtPd).

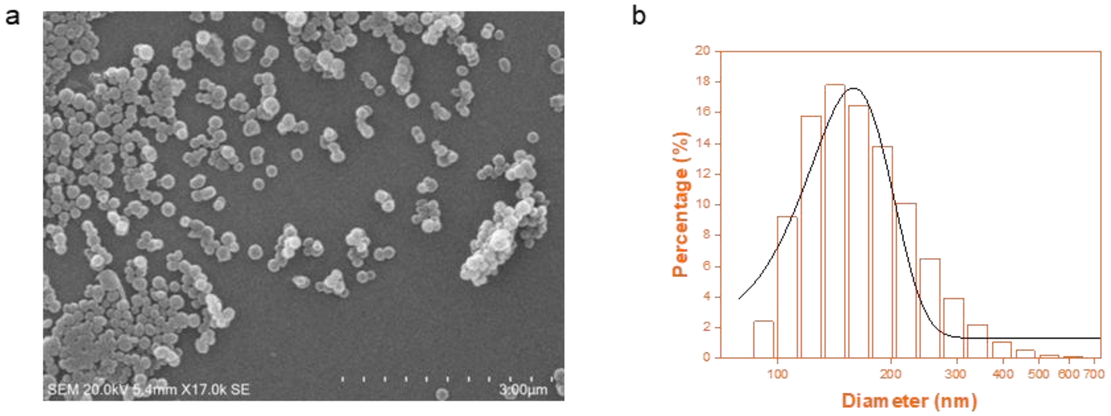

Supplementary Figure 11. (a) SEM image and (b) the corresponding particle size distribution of PCN(PtPd)-Lac calculated using software Nano Measurer 1.2.

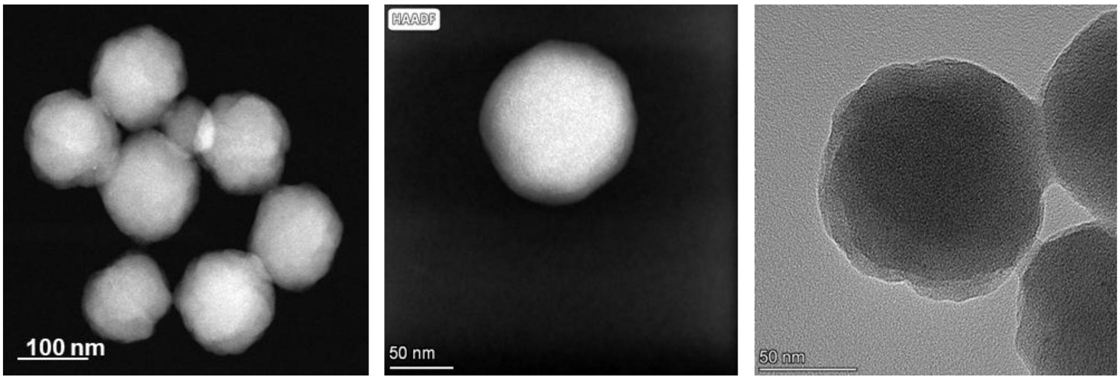

Supplementary Figure 12. Representative TEM images of PCN(PtPd)-Lac.

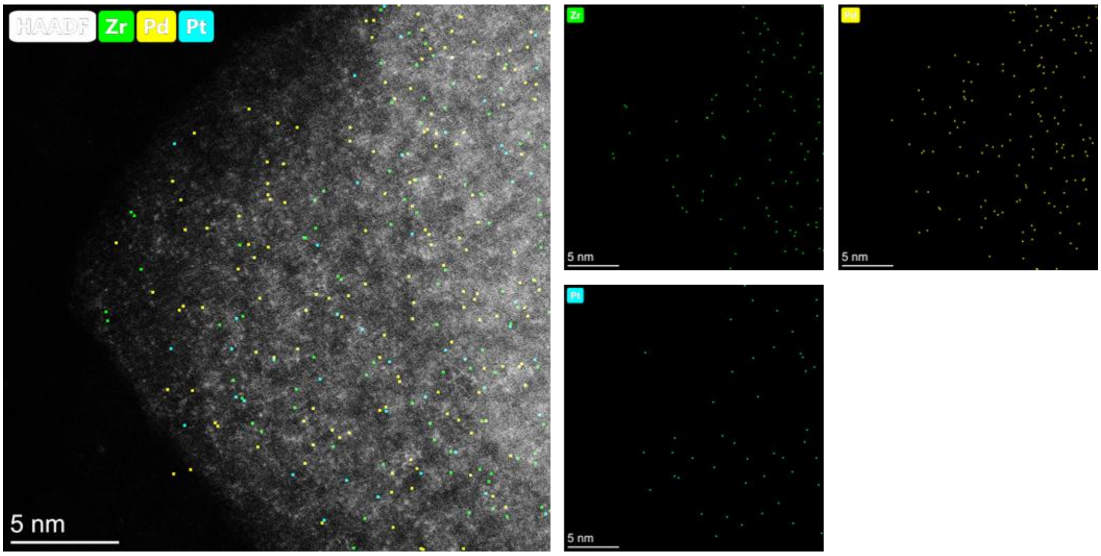

Supplementary Figure 13. AC-STEM of PCN(PtPd) and the corresponding elemental mappings of Zr (green), Pd (yellow), and Pt (cyan).

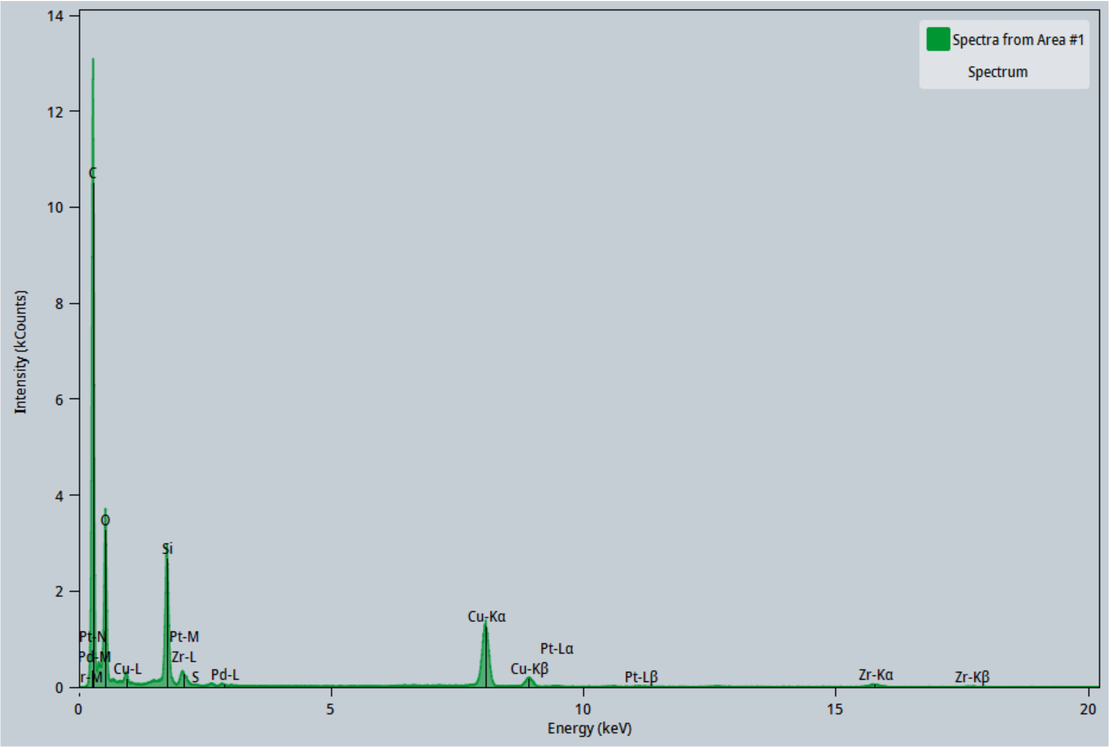

Supplementary Figure 14. EDS spectrum of PCN(PtPd)-Lac.

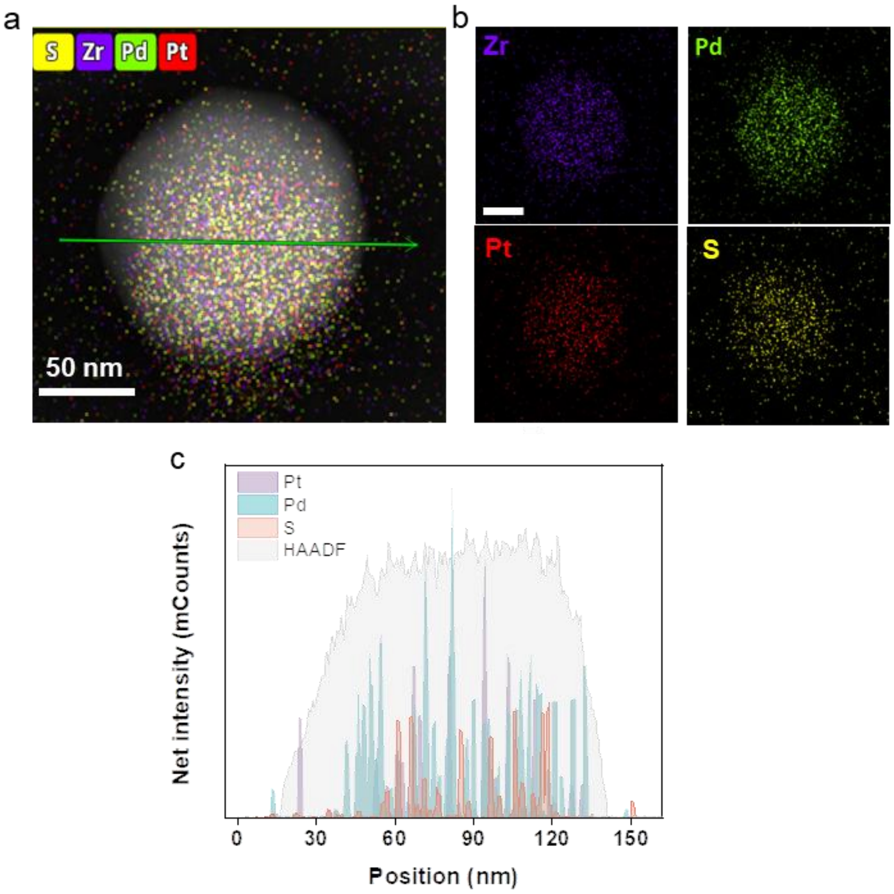

Supplementary Figure 15. (a) HAADF-STEM image of PCN(PtPd)-Lac and (b) the corresponding elemental mappings for Zr, Pt, Pd, and S. Scale bar: 50 nm. (c) Line scan analysis of the distribution of Pt, Pd, and S across the nanoparticle.

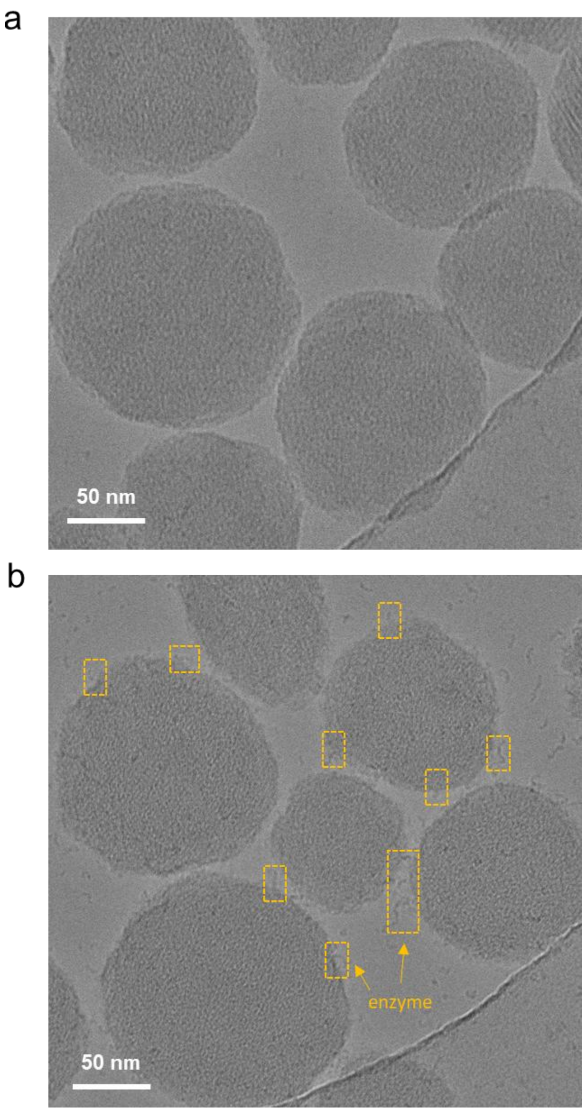

Supplementary Figure 16. (a) Cryo-EM image of PCN(PtPd). **(b)** Cryo-EM image of PCN(PtPd)-Lac, revealing the integration of laccase into the MOF.

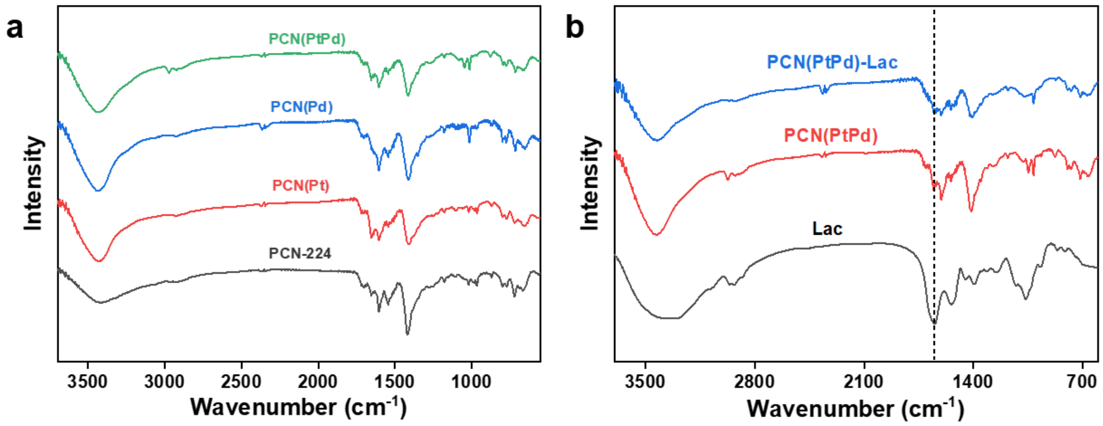

Supplementary Figure 17. (a) FTIR spectra of PCN, PCN(Pt), PCN(Pd), and PCN(PtPd). (b) FTIR spectra of Lac, PCN(PtPd), and PCN(PtPd)-Lac. Compared to PCN(PtPd), the FTIR spectrum of PCN(PtPd)-Lac showed an increased intensity of the characteristic peak at 1655 cm^{-1} that attributed to the C-N stretching and N-H bending vibrations from laccase, indicating the successful immobilization of laccase on PCN(PtPd).

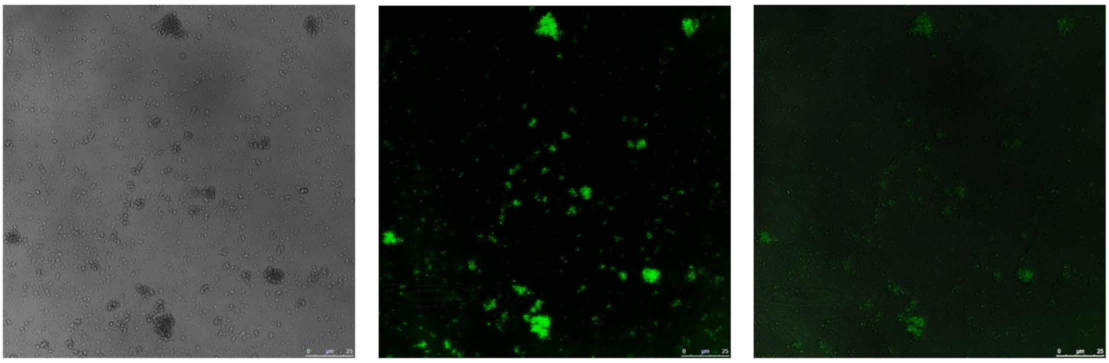

Supplementary Figure 18. CLSM images of PCN(PtPd)-Lac using green fluorescent probe fluorescein isothiocyanate (FITC)-labeled Lac.

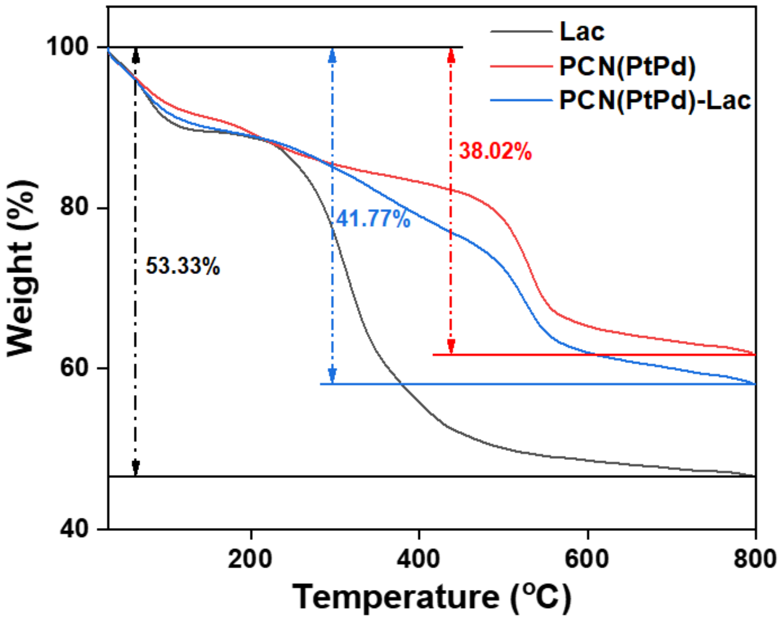

Supplementary Figure 19. Thermogravimetric analysis (TGA) curves of Lac, PCN(PtPd), and PCN(PtPd)-Lac. The TGA curves show the weight loss of Lac, PCN(PtPd), and PCN(PtPd)-Lac as a function of temperature, indicating the thermal stability and the composition of each material. The percentage weight loss for each sample is marked, highlighting the differences in thermal decomposition between the catalysts and the enzyme.

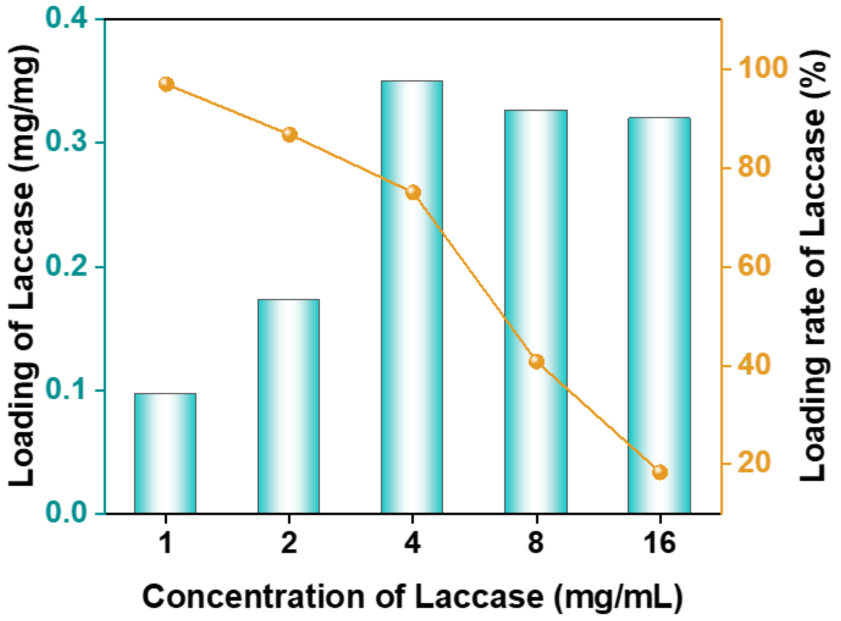

Supplementary Figure 20. Loading amount and loading rate of laccase on PCN(PtPd)-Lac synthesized with different concentration of laccase.

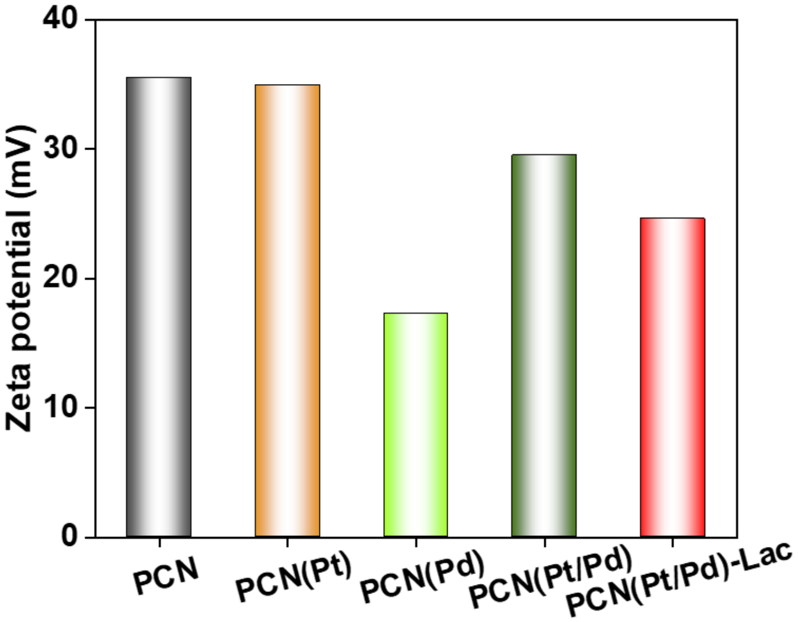

Supplementary Figure 21. Zeta potential measurements of PCN, PCN(Pt), PCN(Pd), PCN(PtPd), and PCN(PtPd)-Lac. Compared with PCN(PtPd), the zeta potential of PCN(PtPd)-Lac decreased because of the incorporation of enzymes.

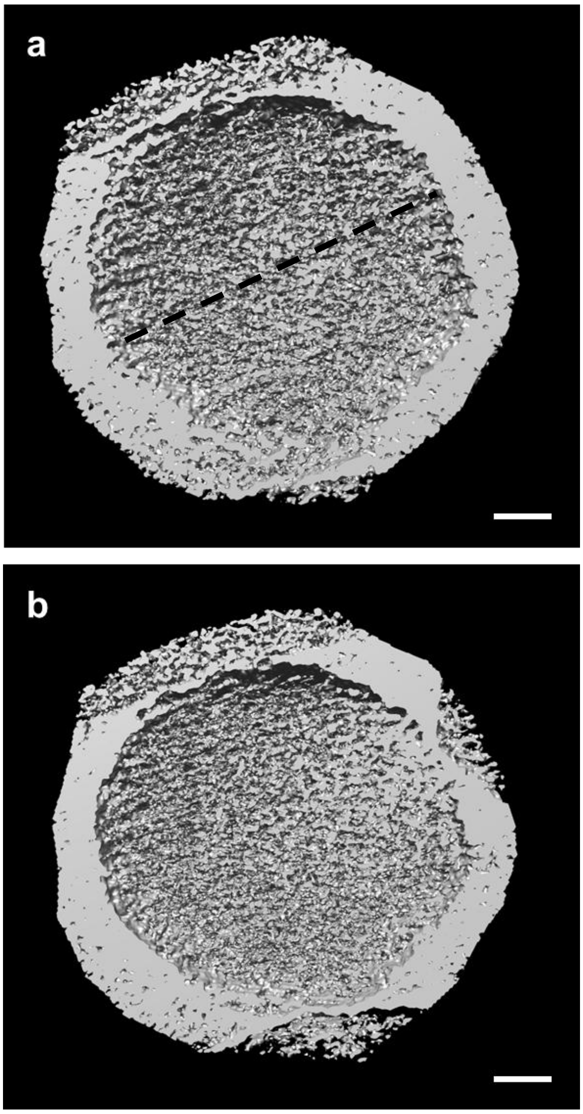

Supplementary Figure 22. Representative Cryo-ET images of PCN(PtPd). The cross-section of PCN(PtPd) displayed mesopores plainly distributed inside the particle. The scale bars are 30 nm.

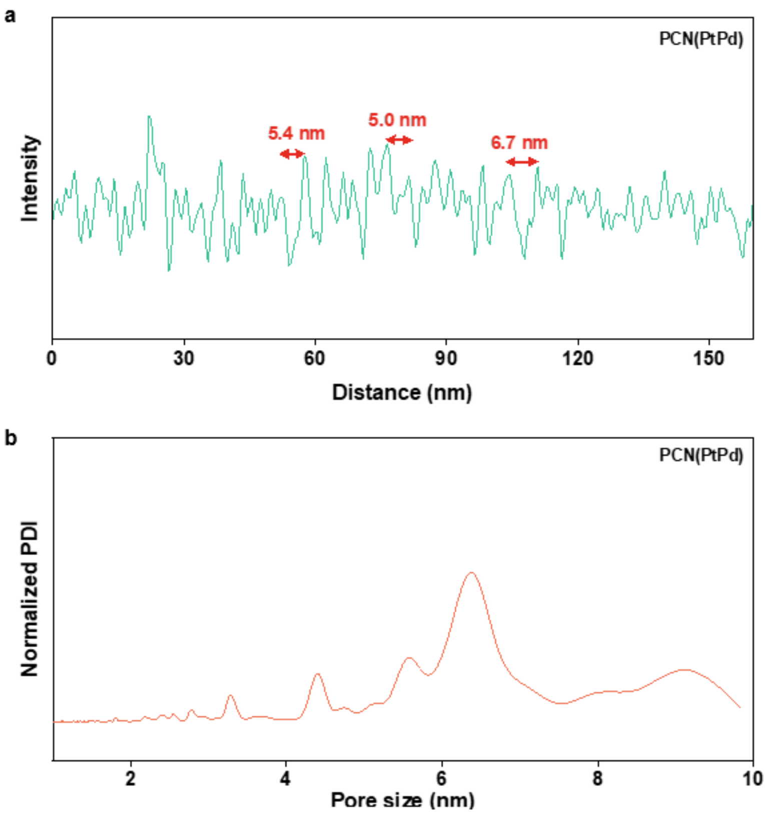

Supplementary Figure 23. (a) Linear scan of electron density along the dashed line in the cryo-ET image of PCN(PtPd) shown in supplementary figure 22. Three characteristic pore sizes are shown on the plot, with peaks possibly representing the pore sizes of PCN(PtPd) marked by arrowheads. (b) Fast Fourier transformation (FFT) of the electron density linear scan is converted to the pore size distribution of PCN(PtPd). Normalized PDI: normalized pore distribution intensity.

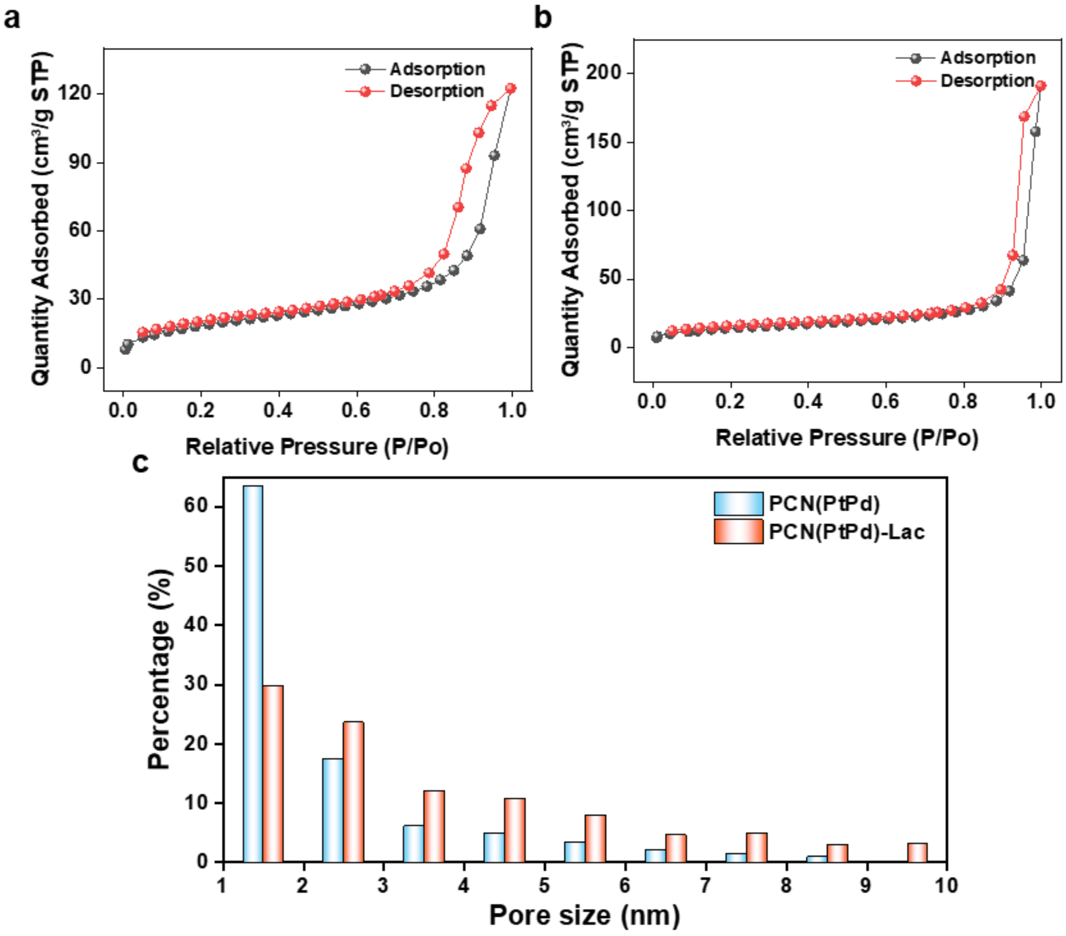

Supplementary Figure 24. BET surface area and pore size distribution of PCN(PtPd) and PCN(PtPd)-Lac. **a,** Nitrogen adsorption-desorption isotherms of PCN(PtPd) and **b,** PCN(PtPd)-Lac. **c,** Pore size distribution of PCN(PtPd) and PCN(PtPd)-Lac, indicating the changes in pore structure due to enzyme loading. The increase in pore size for PCN(PtPd)-Lac suggests enzyme incorporation into the framework.

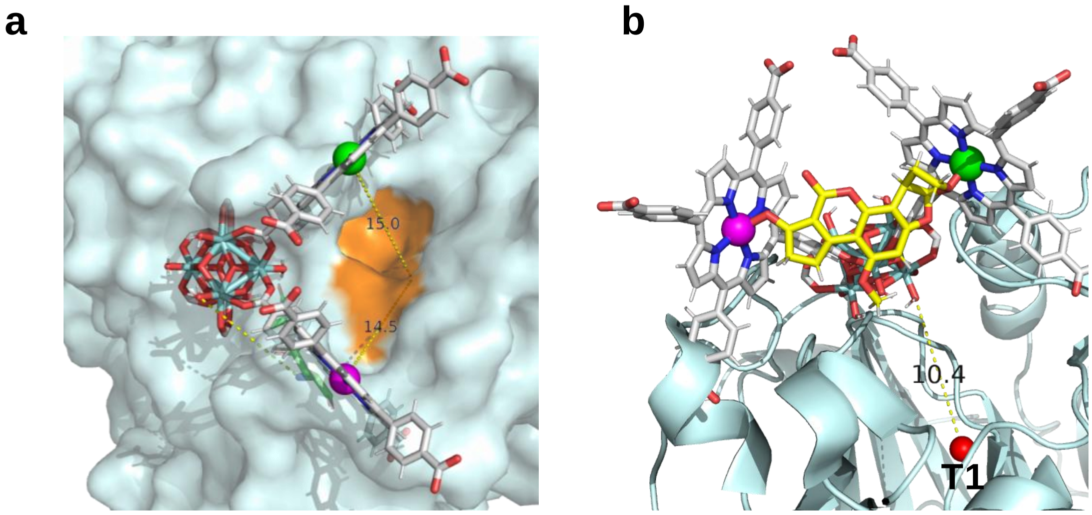

Supplementary Figure 25. The configuration of the hybrid active pocket in PCN(PtPd)-Lac. (a) The distances between metal atoms and active center of laccase (15.0 Å and 14.5 Å). (b) The distance between Zr clusters and T1 copper (T1Cu) center of laccase (10.4 Å)**.**

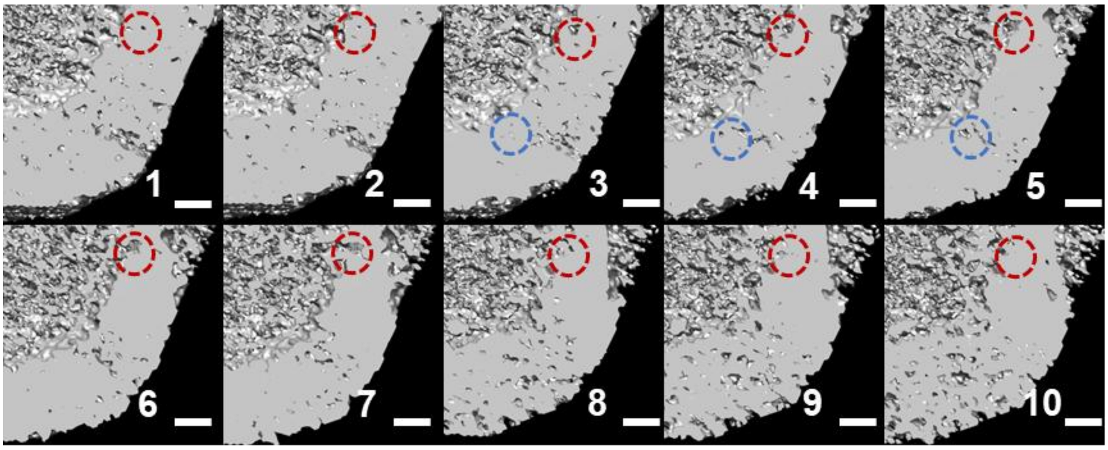

Supplementary Figure 26. A series of cross sections of a single PCN(PtPd) nanocomposite. This series of images suggested that the generated mesopores were interconnected. The scale bars are 10 nm.

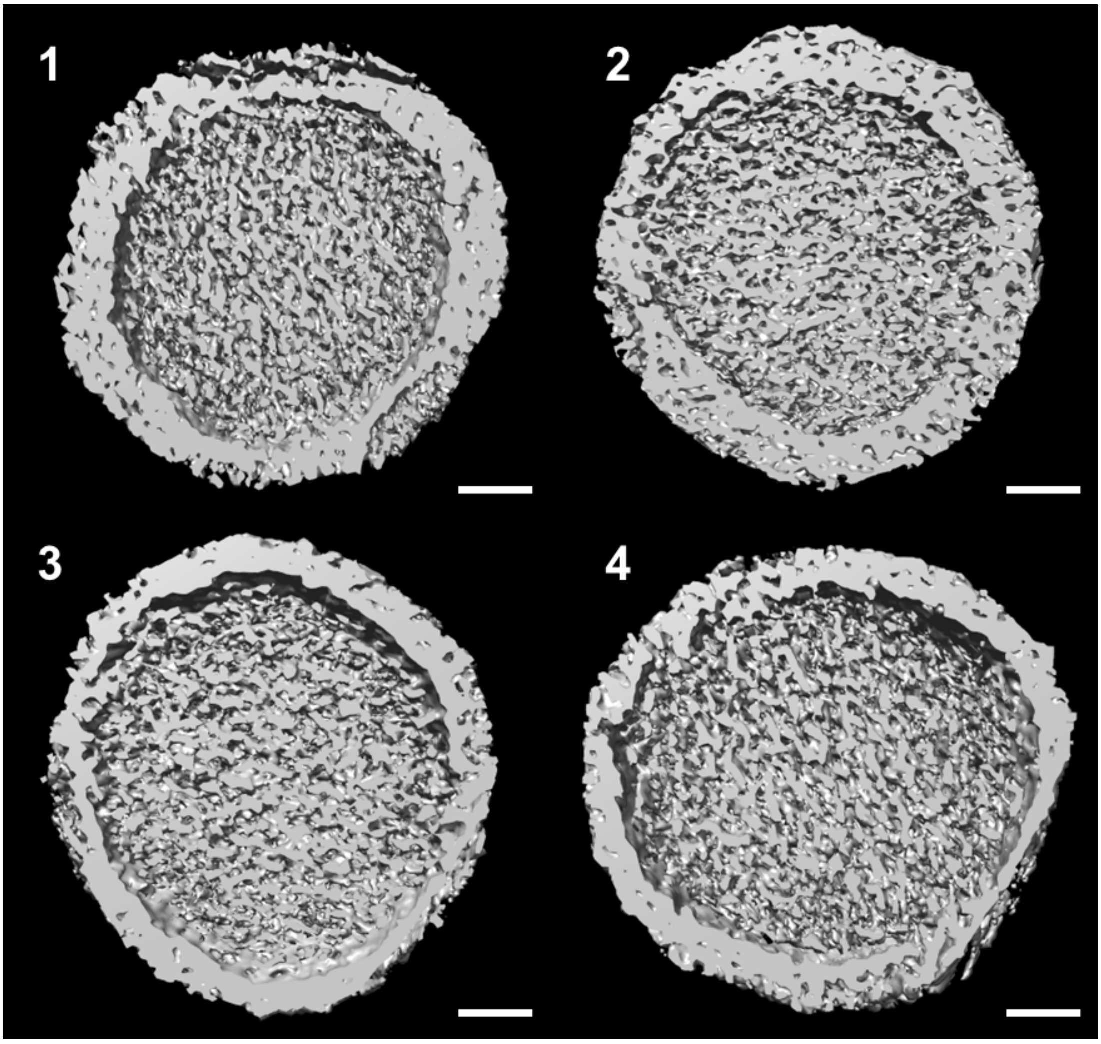

Supplementary Figure 27. Representative Cryo-ET images of PCN(PtPd)-Lac. The scale bars are 30 nm.

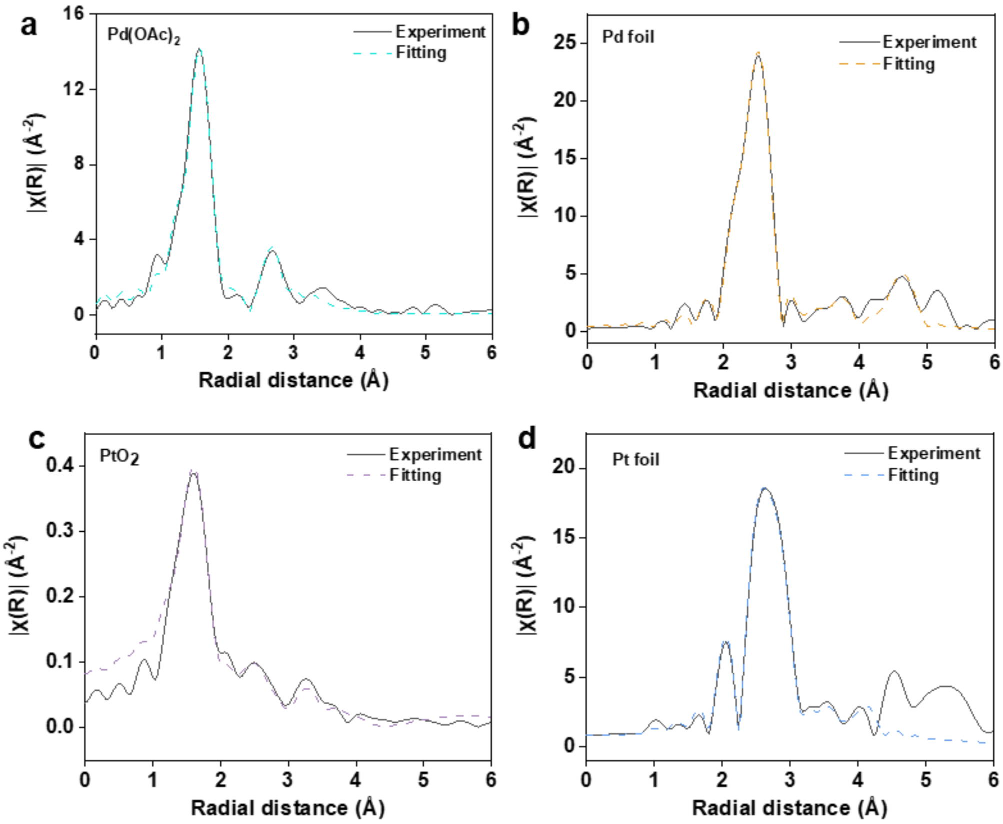

Supplementary Figure 28. Fourier-transformed EXAFS fitting curves in R-space for different reference and experimental samples. (a) $Pd(OAc)_2$, (b) Pd foil, (c) PtO_2, and (d) Pt foil.

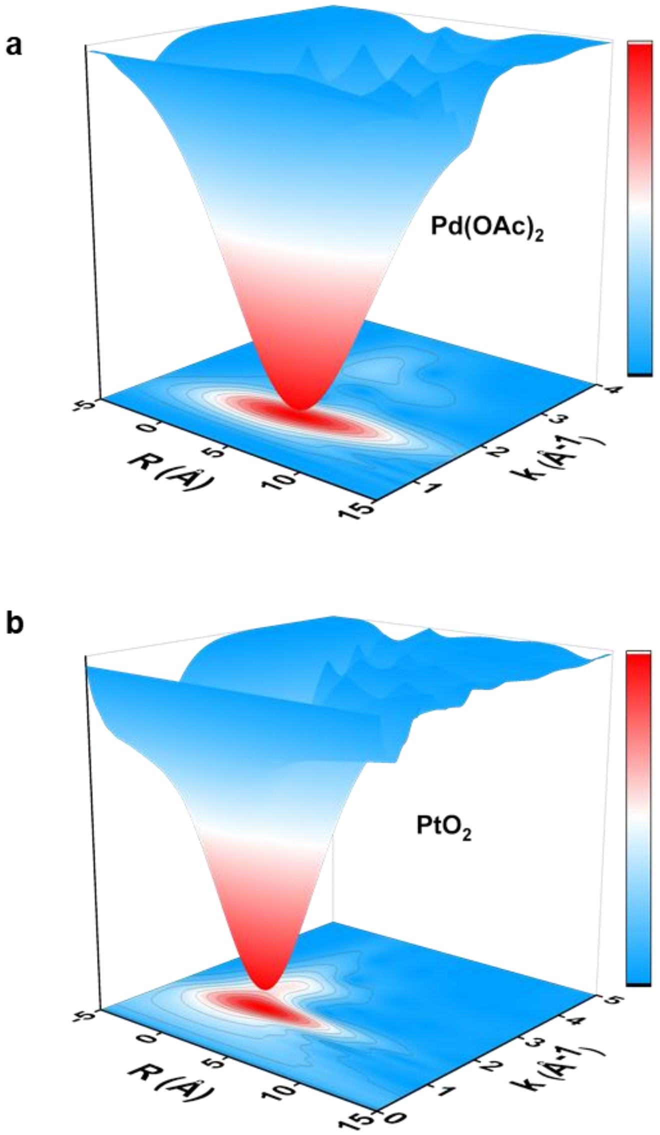

Supplementary Figure 29. 3D contour maps of WT-XAFS spectra: (a) Pd(OAc)$_2$. (b) PtO$_2$.

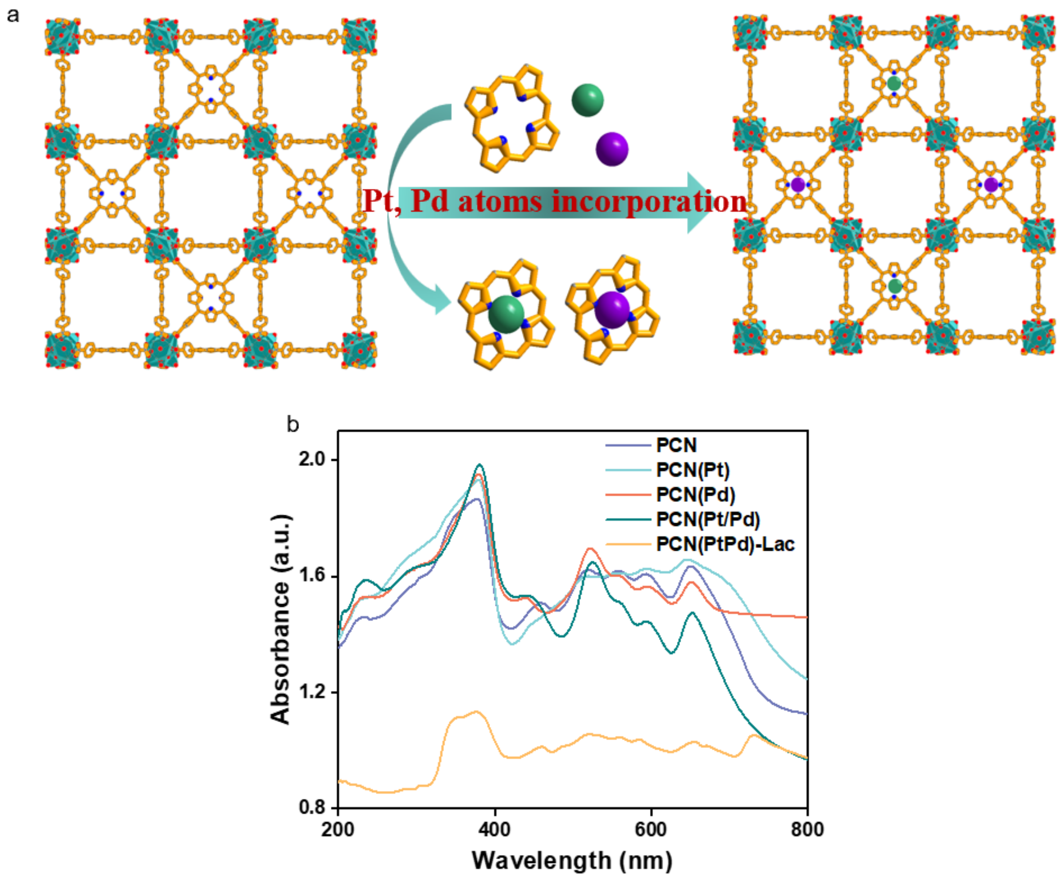

Supplementary Figure 30. (a) Schematic illustration of the incorporation of Pt and Pd atoms into the PCN-224. (b) UV-Vis diffuse reflectance spectra of PCN, PCN(Pt), PCN(Pd), and PCN(PtPd).

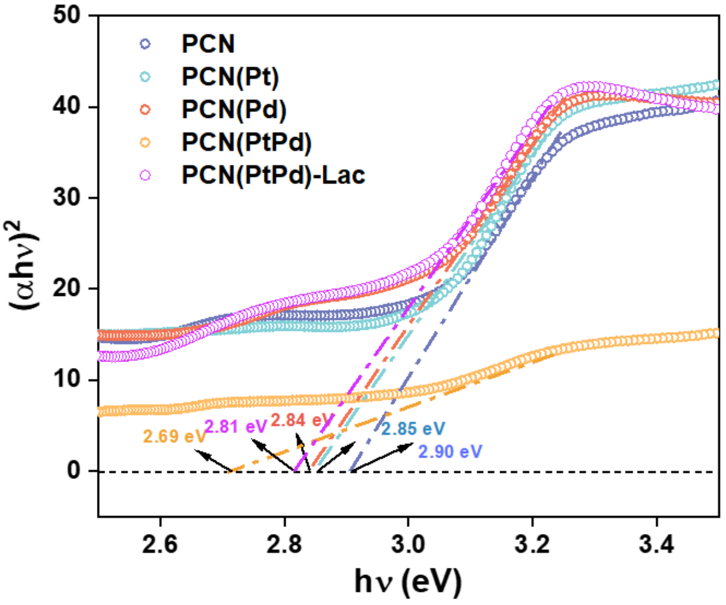

Supplementary Figure 31. Tauc plots for bandgap estimation of PCN, PCN(Pt), PCN(Pd), and PCN(PtPd).

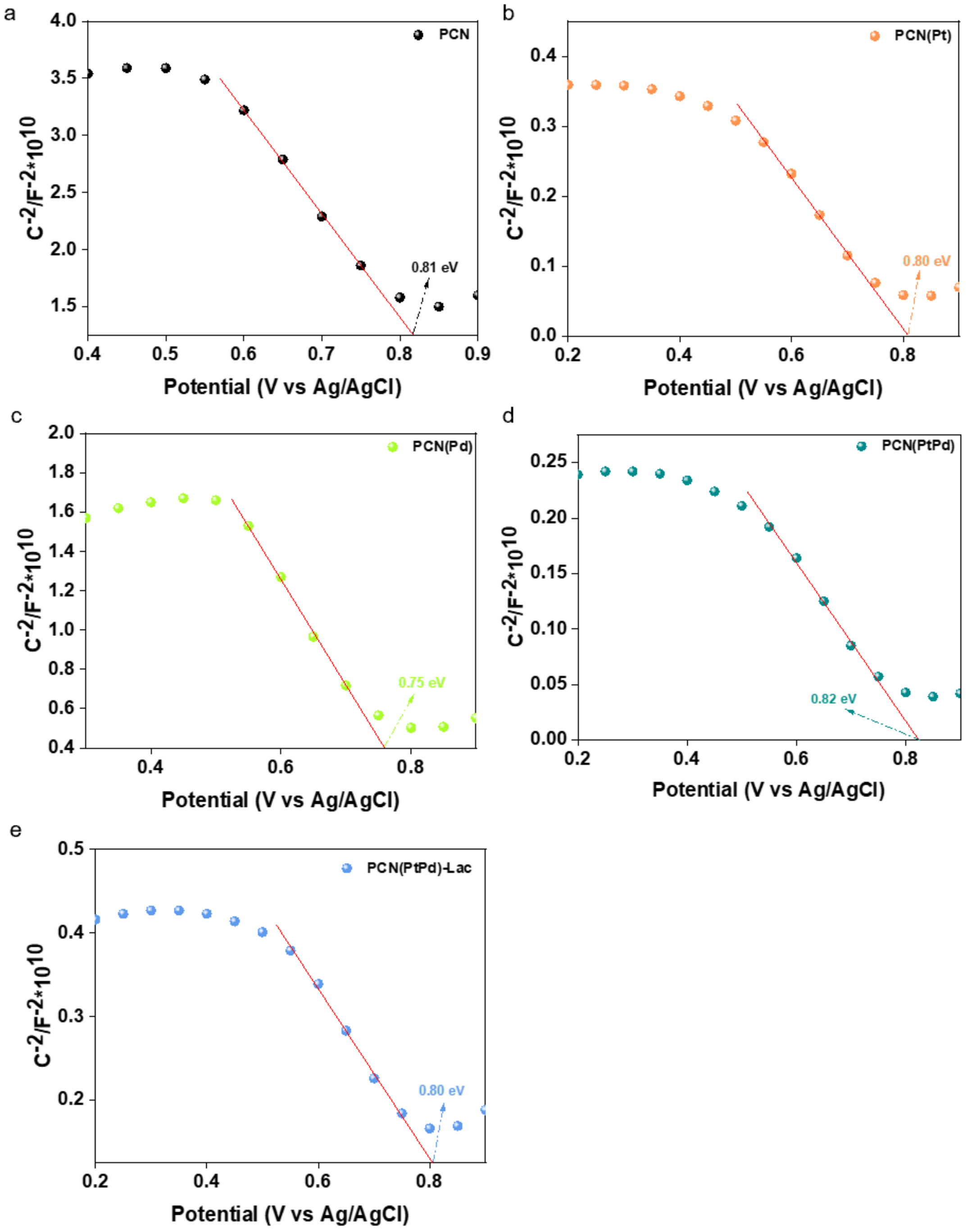

Supplementary Figure 32. Mott-Schottky plots of PCN, PCN(Pt), PCN(Pd), and PCN(PtPd). The Mott-Schottky measurements show the potential versus capacitance squared C^{-2} for each sample, used to determine the flat-band potential. The estimated flat-band potentials are indicated on each plot, revealing slight shifts in the flat-band position due to the incorporation of Pt and Pd, which affects the electronic properties and charge transfer capabilities of the catalysts.

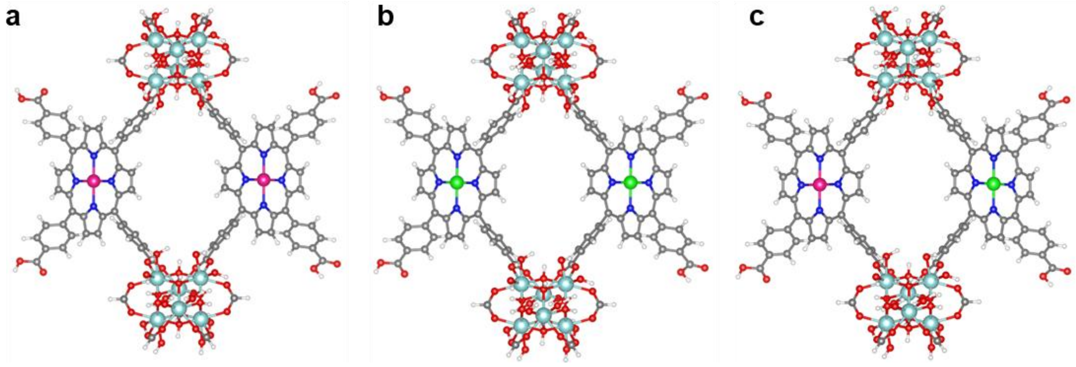

Supplementary Figure 33. DFT-optimized configuration of (a) PCN(Pd), (b) PCN(Pt), and (c) PCN(PtPd). Green: Pt, Pink: Pd.

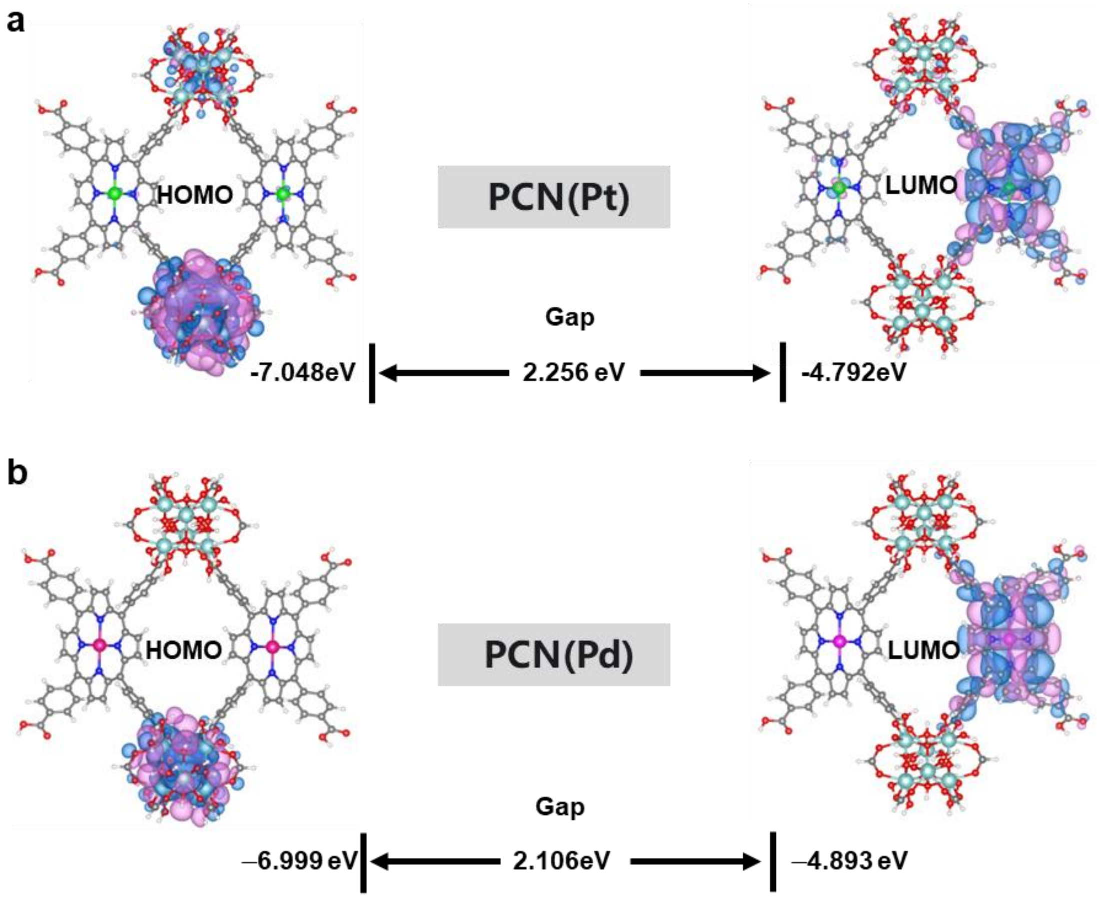

Supplementary Figure 34. The molecular orbital diagrams of (a) PCN(Pt) and (b) PCN(Pd). Green: Pt, Pink: Pd.

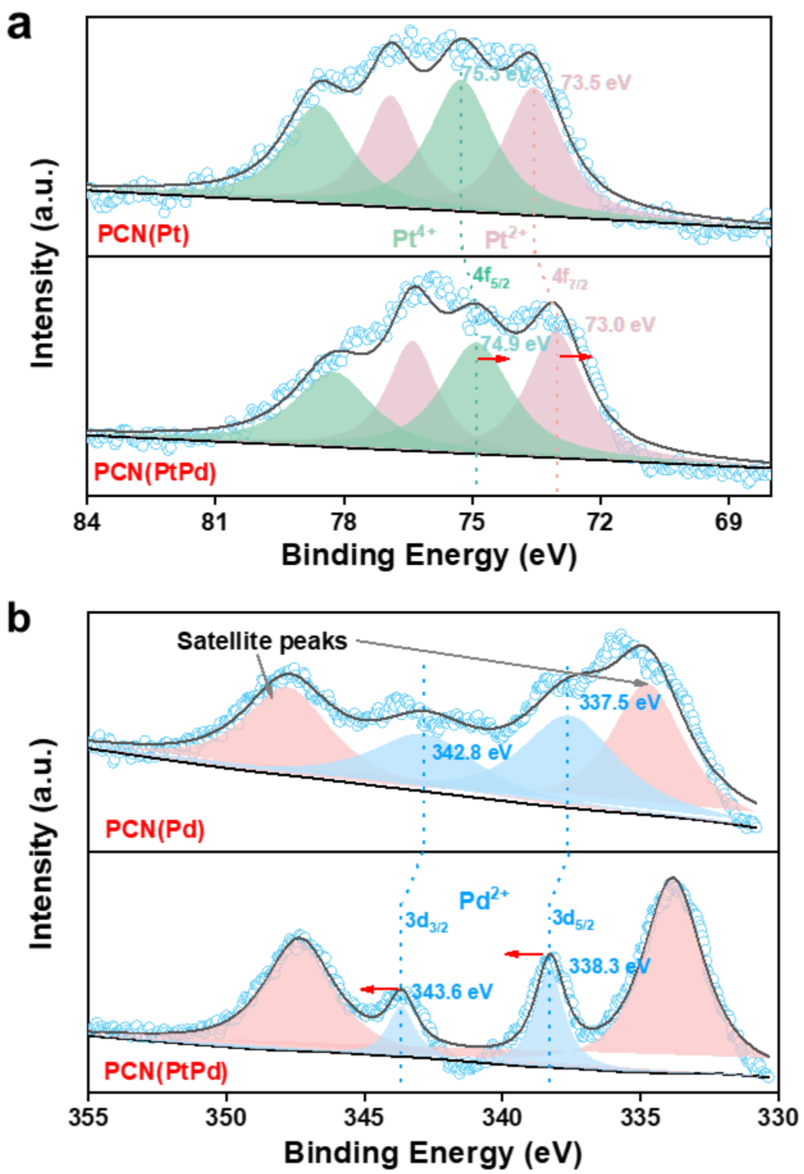

Supplementary Figure 35. (a) Pt 4f XPS spectra of PCN(Pt) and PCN(PtPd). (b) Pd 3d XPS spectra of PCN(Pd) and PCN(PtPd). In Pt 4f XPS, two sets of peaks fitted with spin-orbit split 4f$_{7/2}$ and 4f$_{5/2}$ components were observed, which attributed to the Pt^{2+} and Pt^{4+} species, respectively. The peaks of PCN(PtPd) obviously shift towards the lower binding energy compared with that of PCN(Pt). In Pd 3d XPS, the peaks of PCN(PtPd) displayed a shift towards the higher binding energy compared with that of PCN(Pd), showing that there is subtle electron transfer from Pd to Pt.

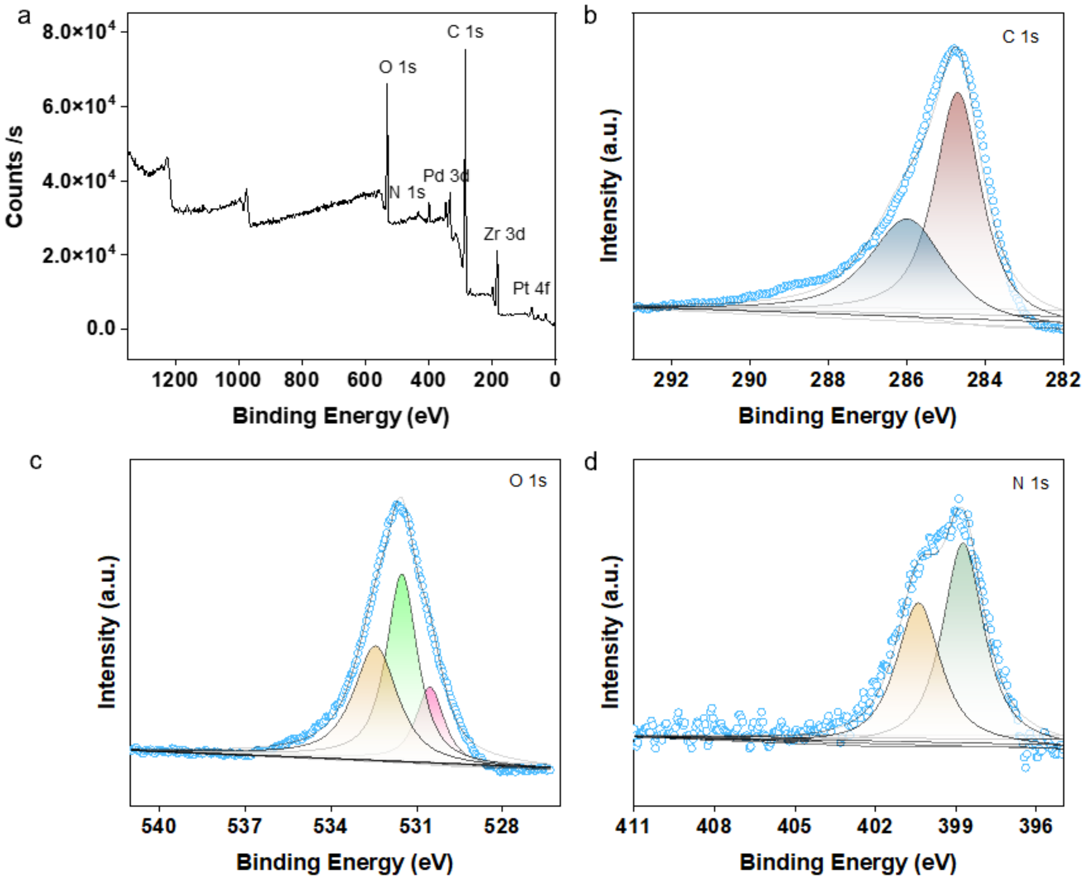

Supplementary Figure 36. XPS spectra of PCN(PtPd). (a) The survey spectrum. (b) C 1s XPS spectrum. (c) O 1s XPS spectrum. (d) N 1s XPS spectrum.

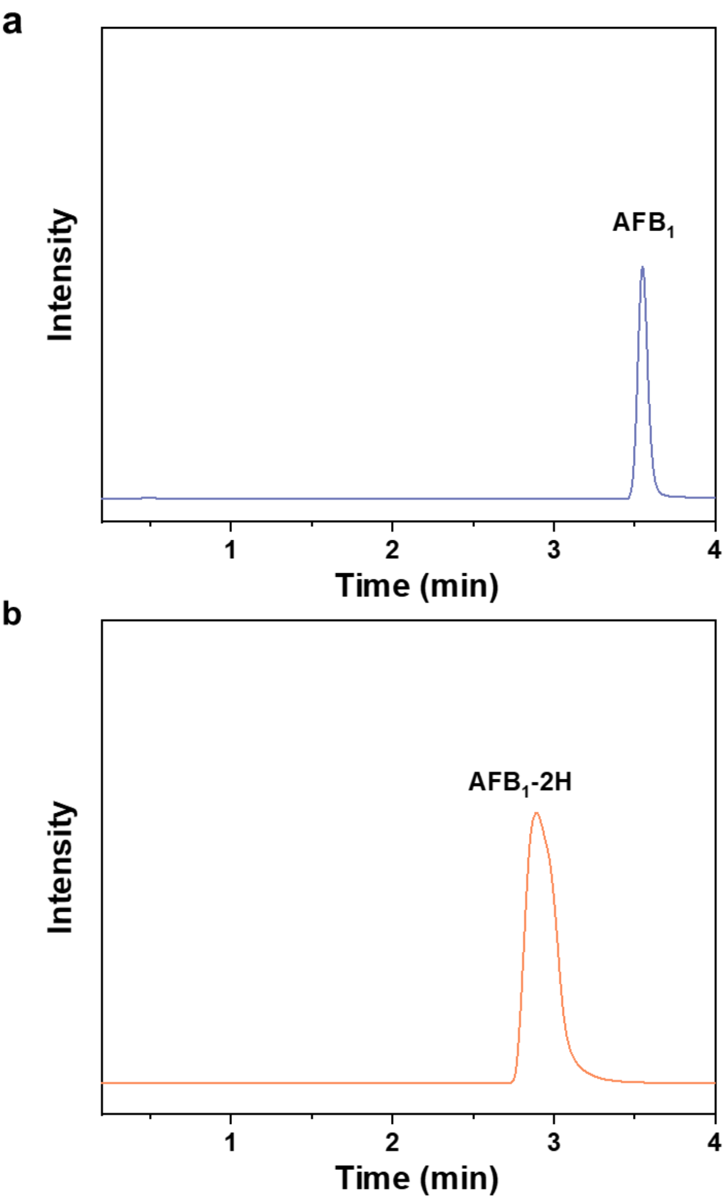

Supplementary Figure 37. HPLC spectra of (a) AFB$_1$, and (b) the reaction solution of the photocatalytic water-donating transfer hydrogenation of AFB$_1$. Conditions: 6 nmol AFB$_1$, 0.01 mg PCN(PtPd), air, 25 ^{o}C under visible light irradiation for 10 min.

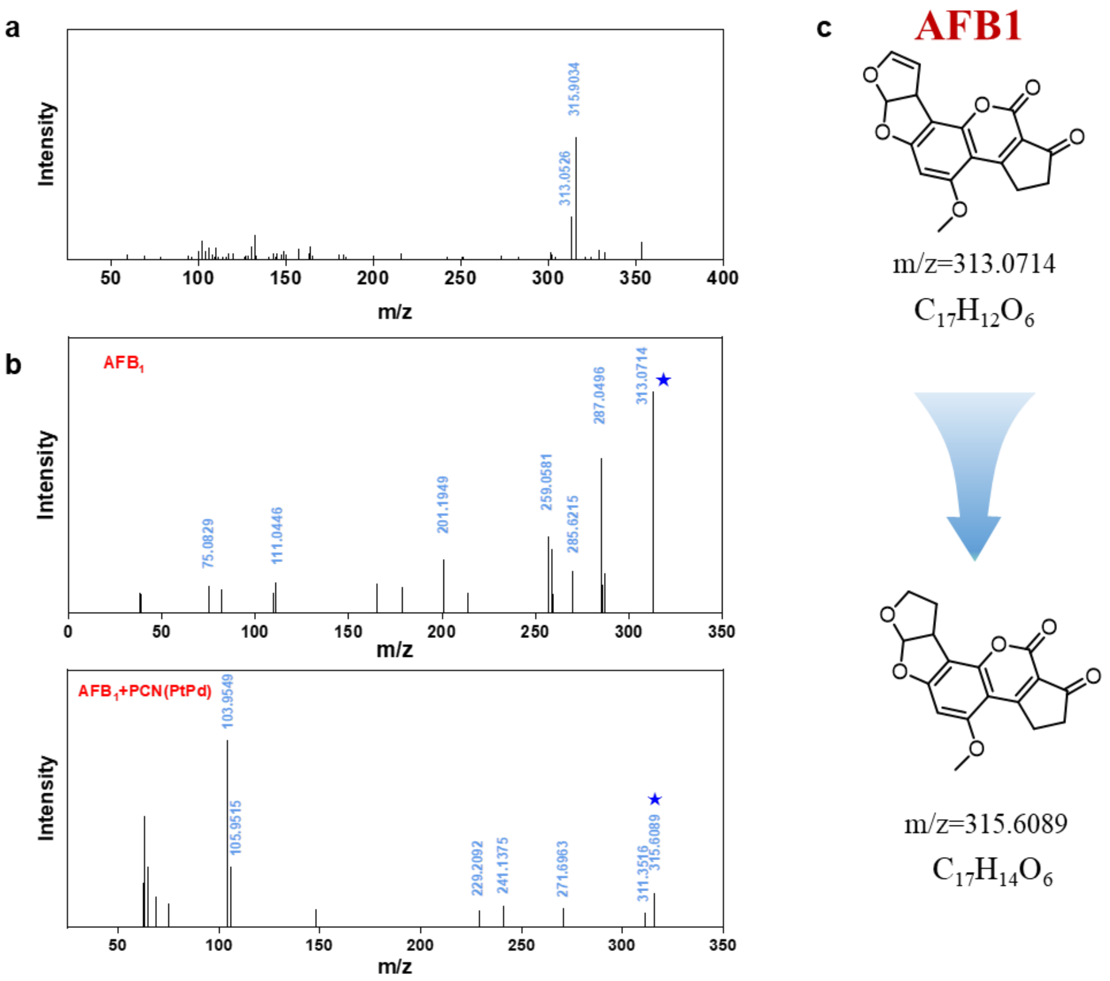

Supplementary Figure 38. (a) MS spectrum of the AFB_1 transformation product in the photocatalytic transfer hydrogenation reaction catalyzed by PCN(PtPd) under visible-light irradiation. (b) MS-MS spectra of AFB_1 and the transformation product. (c) Structure of AFB_1 transformation product.

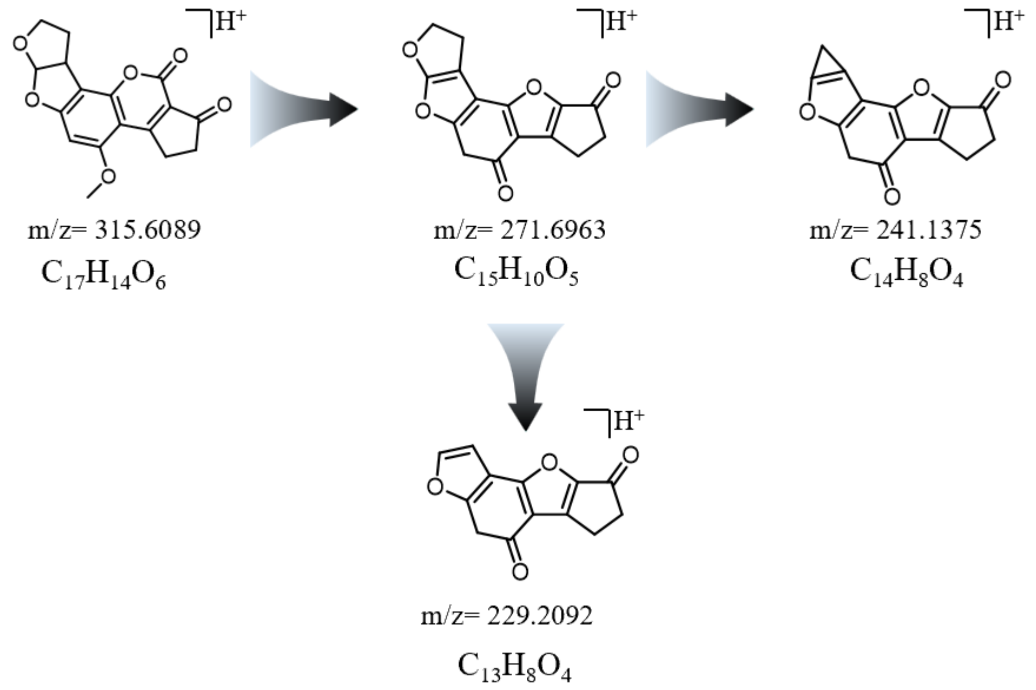

Supplementary Figure 39. Fragmentation pathway of the AFB_1 transformation product in the photocatalytic transfer hydrogenation reaction catalyzed by PCN(PtPd) under visible light irradiation monitored by UPLC-QTOF-MS.

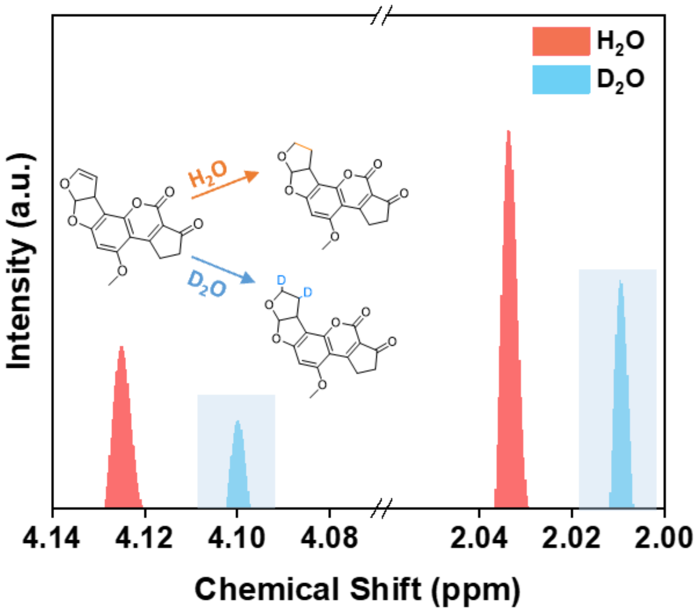

Supplementary Figure 40. Change in the ^{1}HNMR spectra of the AFB$_1$ transformation products catalyzed by PCN(PtPd)-Lac using H_2O and D_2O as the solvent, respectively.

^1H NMR (400 MHz, $CDCl_3$) δ 6.80 (s, 1H), 6.42 (s, 1H), 5.48 (s, 1H), 4.77 (s, 1H), 4.10 (s, 2H), 3.95 (s, 3H), 3.40 (s, 1H), 2.65 (s, 2H), 2.01 (s, 2H).

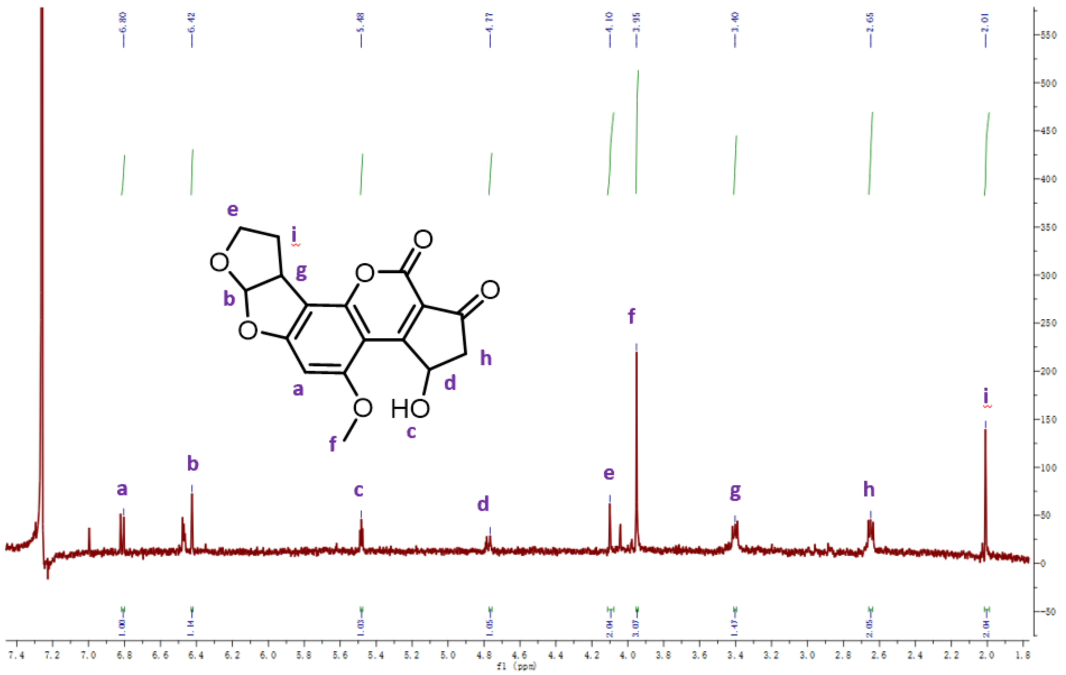

Supplementary Figure 41. ^1H NMR spectrum of the AFB_1 transformation product catalyzed by PCN(PtPd)-Lac using H_2O as the solvent under visible light irradiation.

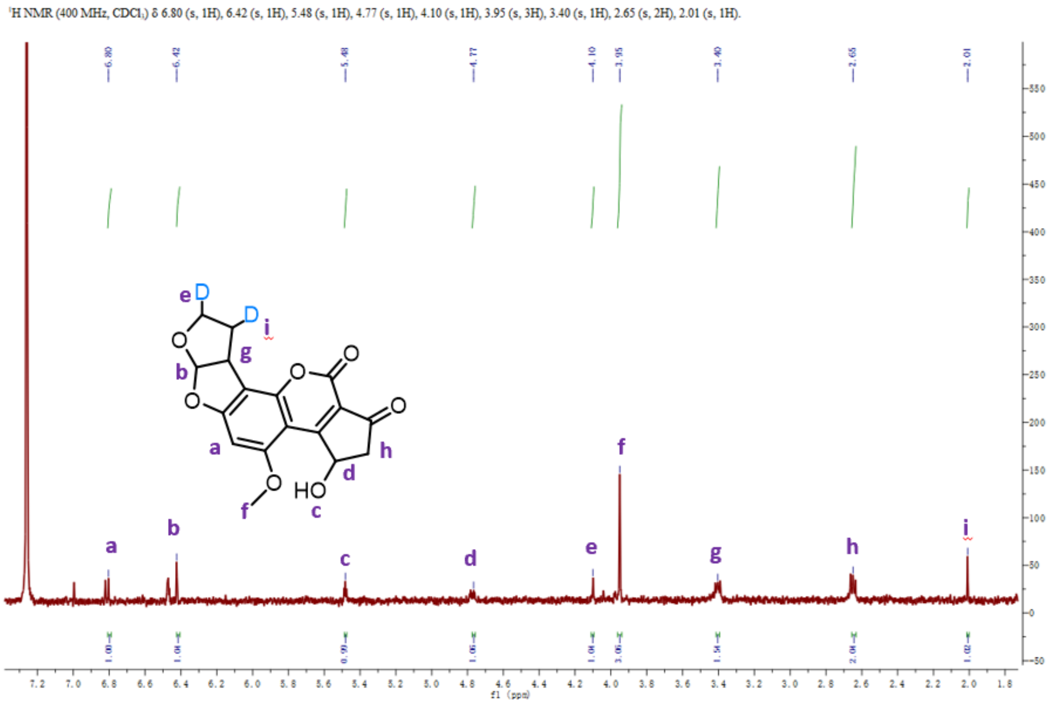

Supplementary Figure 42. ^{1}H NMR spectrum of the AFB$_1$ transformation product catalyzed by PCN(PtPd)-Lac using D$_2$O as the solvent under visible light irradiation.

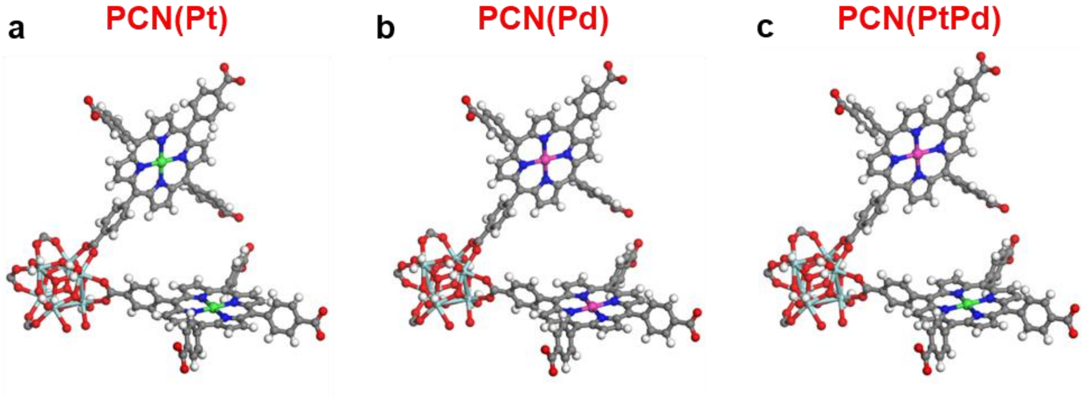

Supplementary Figure 43. The optimized structures of (a) PCN(Pt), (b) PCN(Pd), and (c) PCN(PtPd).

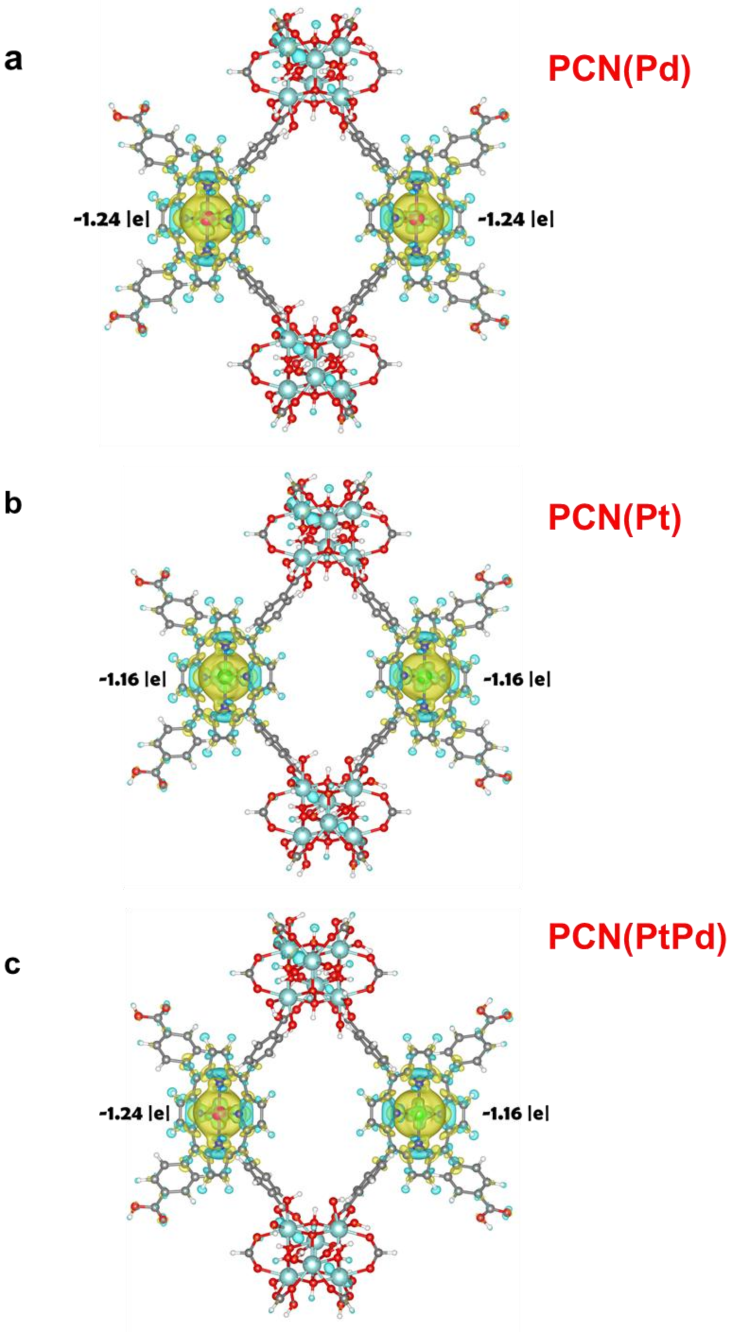

Supplementary Figure 44. Isosurface (level 0.003) of charge difference on (a) PCN-224 with Pd(II), (b) PCN-224 with Pt(II), and (c) PCN-224 with Pd(II) and Pt(II) calculated by DFT. Yellow indicates electron accumulation, and light blue indicates depletion. The minus sign indicates electron accumulation.

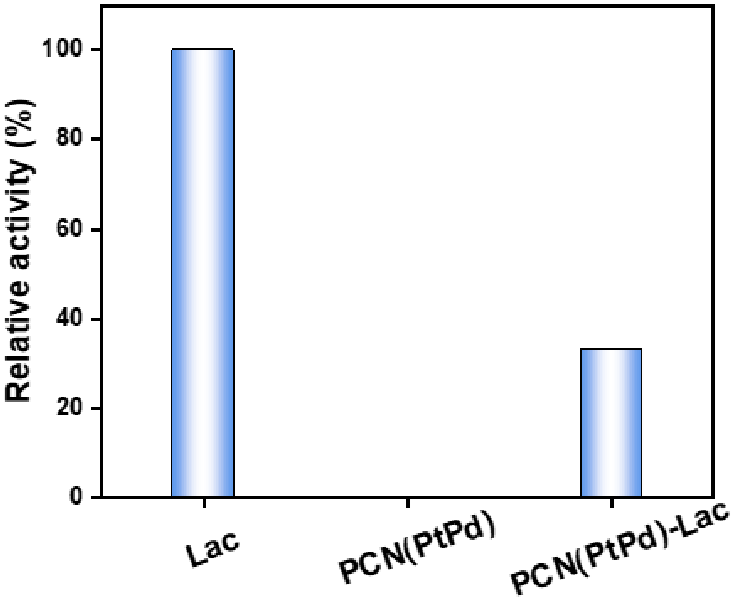

Supplementary Figure 45. Relative activity of free Laccase, PCN(PtPd), and PCN(PtPd)-Lac in the oxidation of TMB.

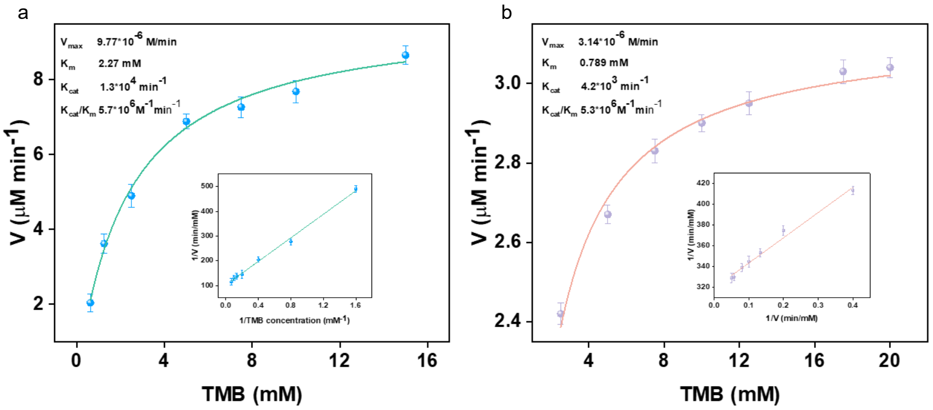

	Lac	**PCN(PtPd)-Lac**
V_{max}(M/min)	9.77*10^{-6}	3.14*10^{-6}
K_m(mM)	2.27	0.789
K_{cat}(min^{-1})	1.3*10^4	4.2*10^3
K_{cat}/K_m(M^{-1}min^{-1})	5.7*10^6	5.3*10^6

Supplementary Figure 46. The kinetics parameters of (a) Lac and (b) PCN(PtPd)-Lac.

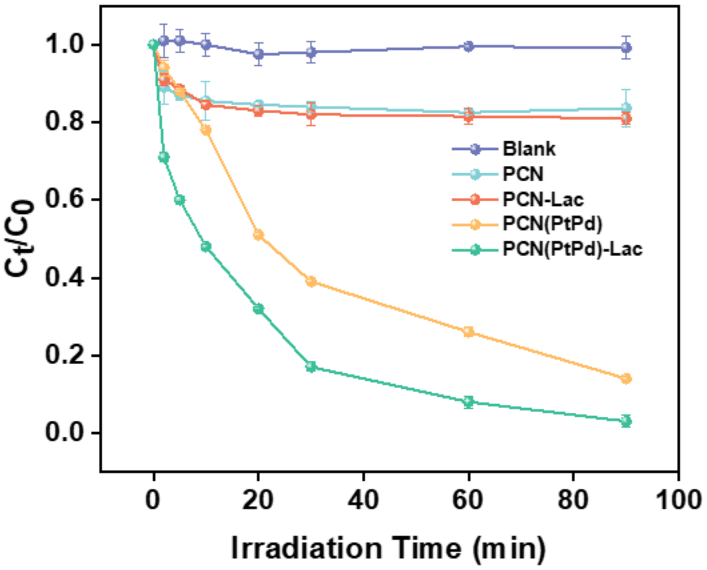

Supplementary Figure 47. Catalytic performances of PCN, PCN-Lac, PCN(PtPd), and PCN(PtPd)-Lac in the degradation of AFB_1. C_t and C_0 are the AFB_1 concentrations after and before the reaction, respectively. Conditions: 6 nmol mycotoxins, 0.01 mg PCN(PtPd)-Lac, 1 mL H_2O, 25 °C under visible-light irradiation. The decrease in AFB_1 concentration in the reaction catalyzed by PCN and PCN-Lac due to the adsorption.

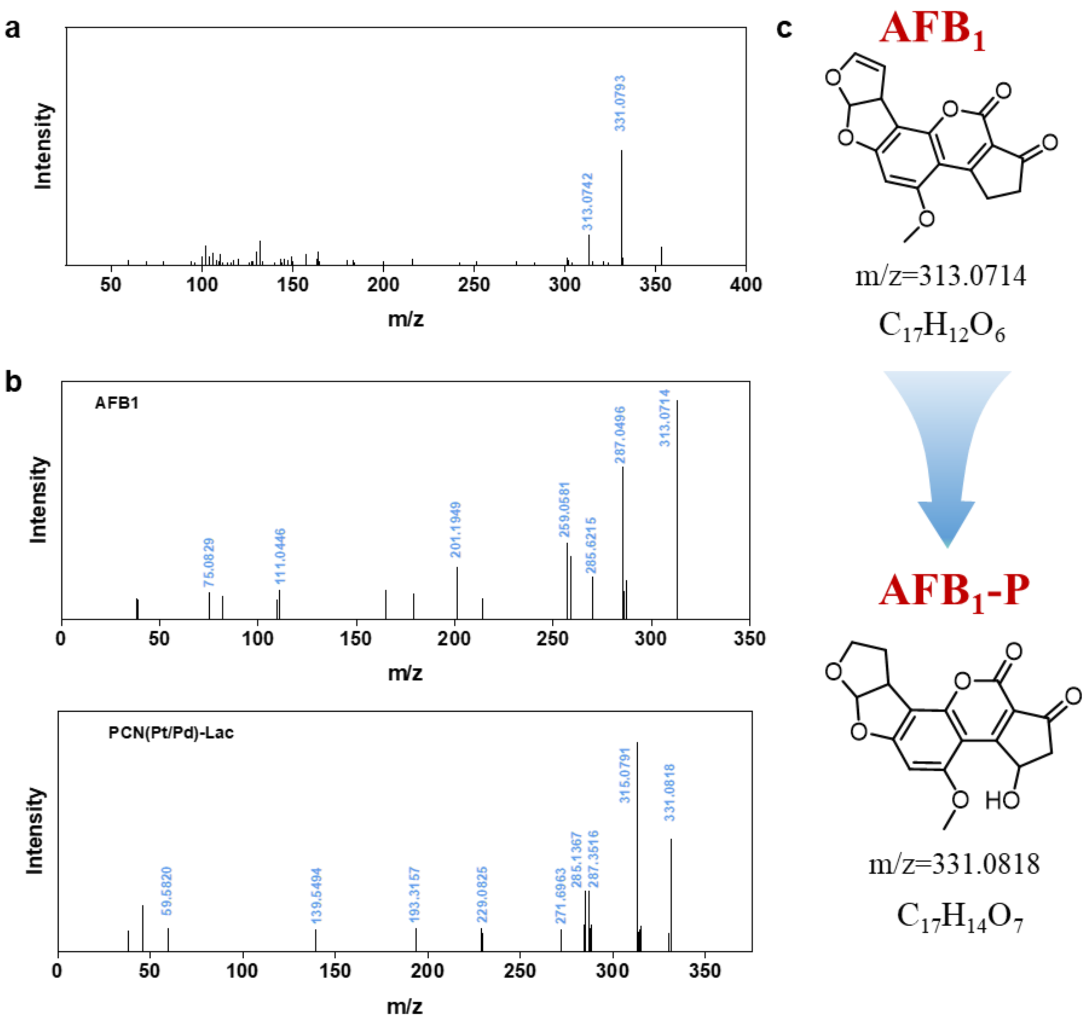

Supplementary Figure 48. (a) MS spectrum of AFB1 transformation product. (b) MS-MS spectra of AFB1 and transformation product. (c) Structure of AFB1 transformation product.

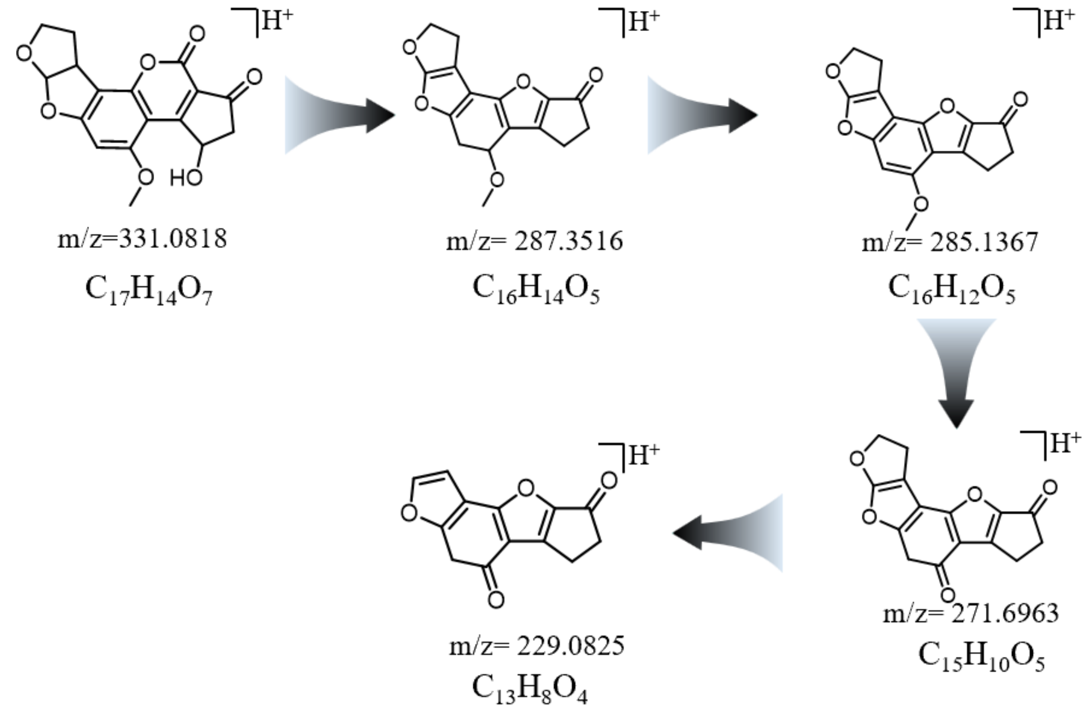

Supplementary Figure 49. Fragmentation pathway of AFB_1 transformation product in UPLC-QTOF-MS.

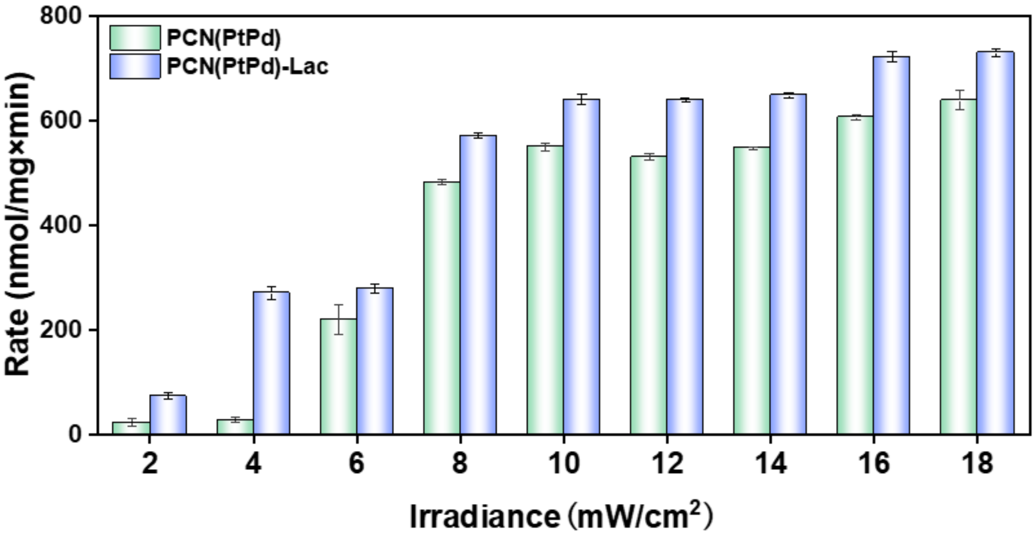

Supplementary Figure 50. Effect of light intensity on the catalytic performance of PCN(PtPd) and PCN(PtPd)-Lac in the degradation AFB_1.

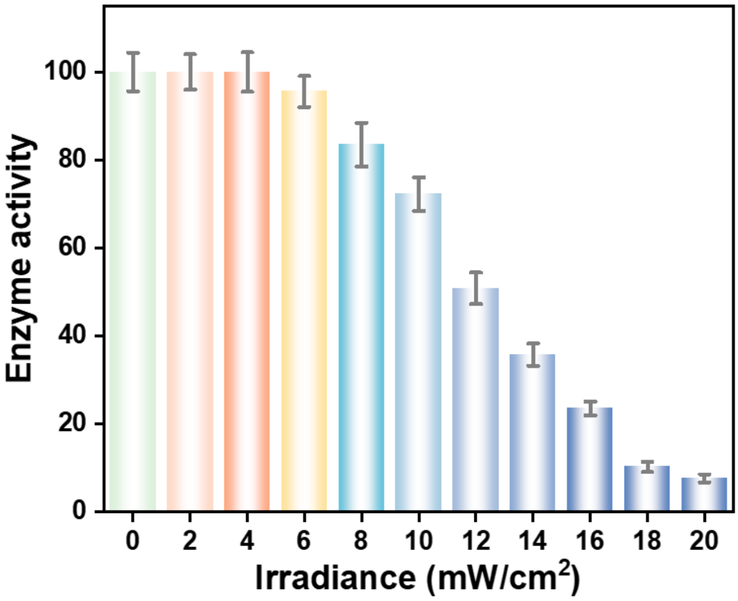

Supplementary Figure 51. Effect of light intensity on the catalytic performance of PCN(PtPd) and PCN(PtPd)-Lac in the degradation AFB_1.

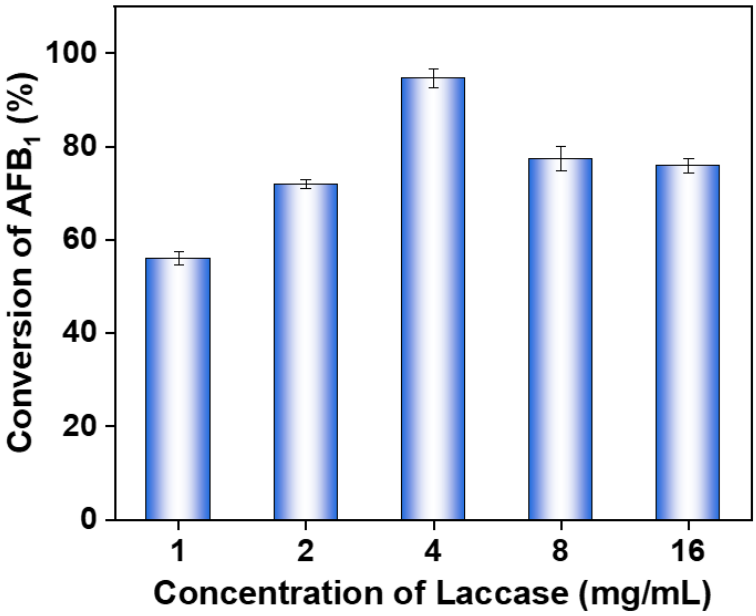

Supplementary Figure 52. The conversion of AFB$_1$ catalyzed by PCN(PtPd)-Lac synthesized with different concentration of laccase.

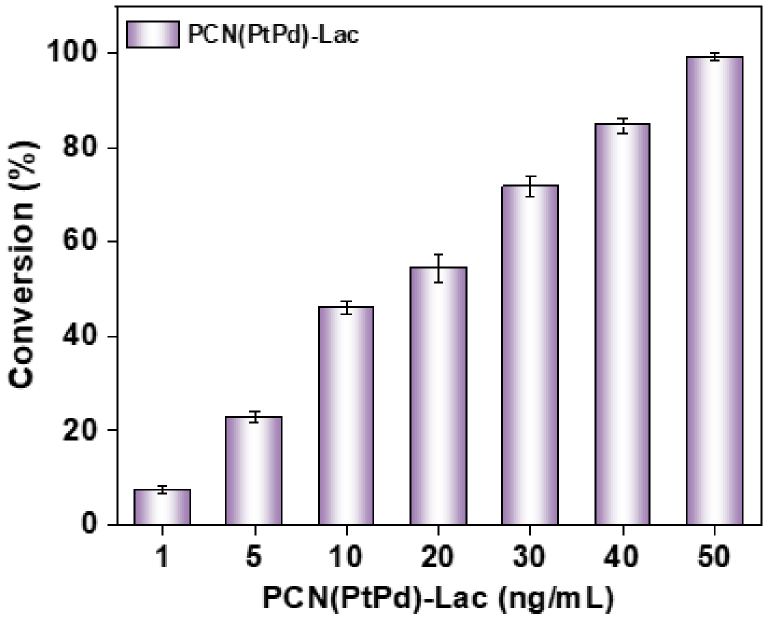

Supplementary Figure 53. Effect of PCN(PtPd)-Lac dosage on AFB_1 degradation efficiency.

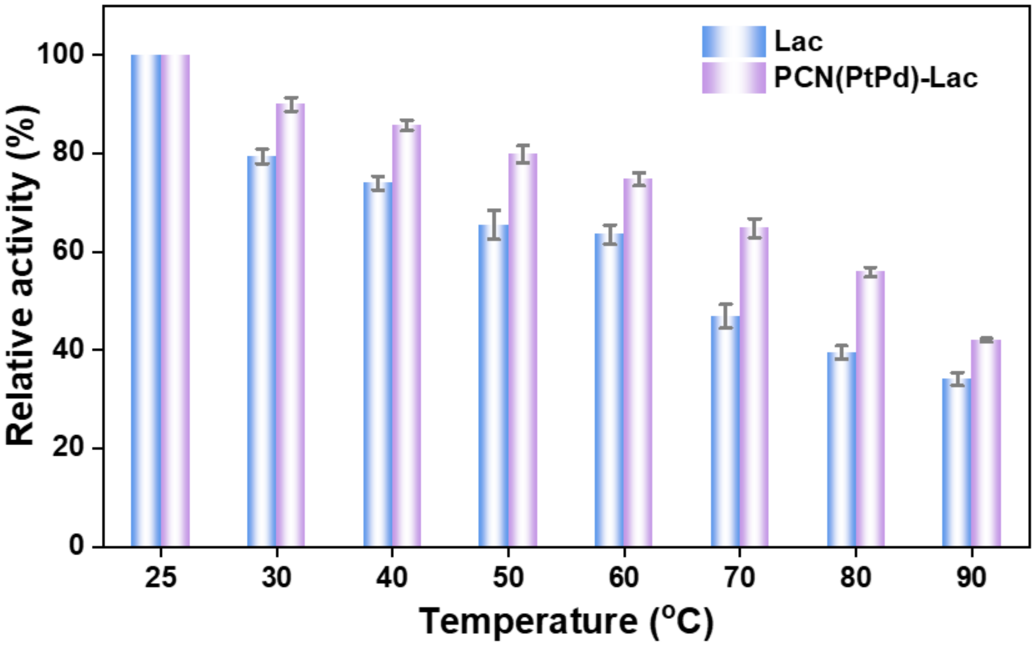

Supplementary Figure 54. Thermal stability of free laccase (Lac) and PCN(PtPd)-Lac. The graph shows the relative stability (%) of free laccase and PCN(PtPd)-Lac after treatment at different temperatures (25–90°C) for 30 minutes. PCN(PtPd)-Lac exhibits higher thermal stability compared to free laccase, maintaining over 50% of its activity up to 70°C.

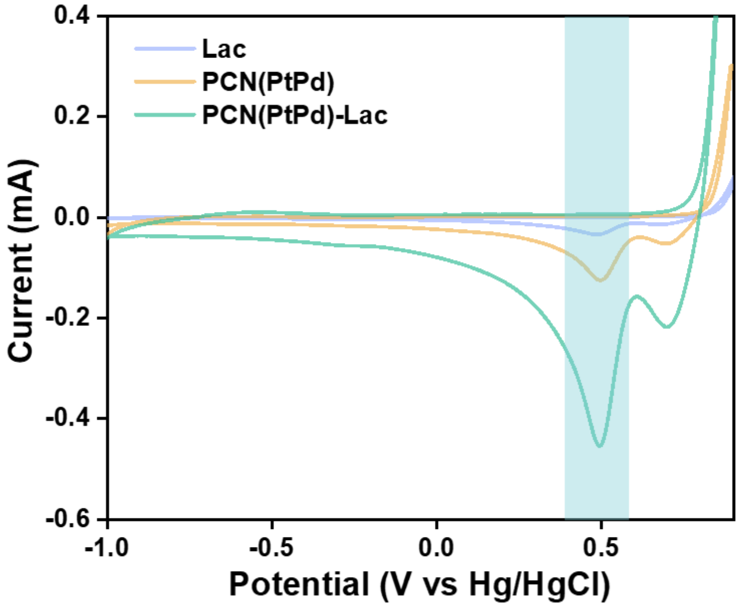

Supplementary Figure 55. The redox reaction potentials of Lac, PCN(PtPd), and PCN(PtPd)-Lac measured by cyclic voltammetry.

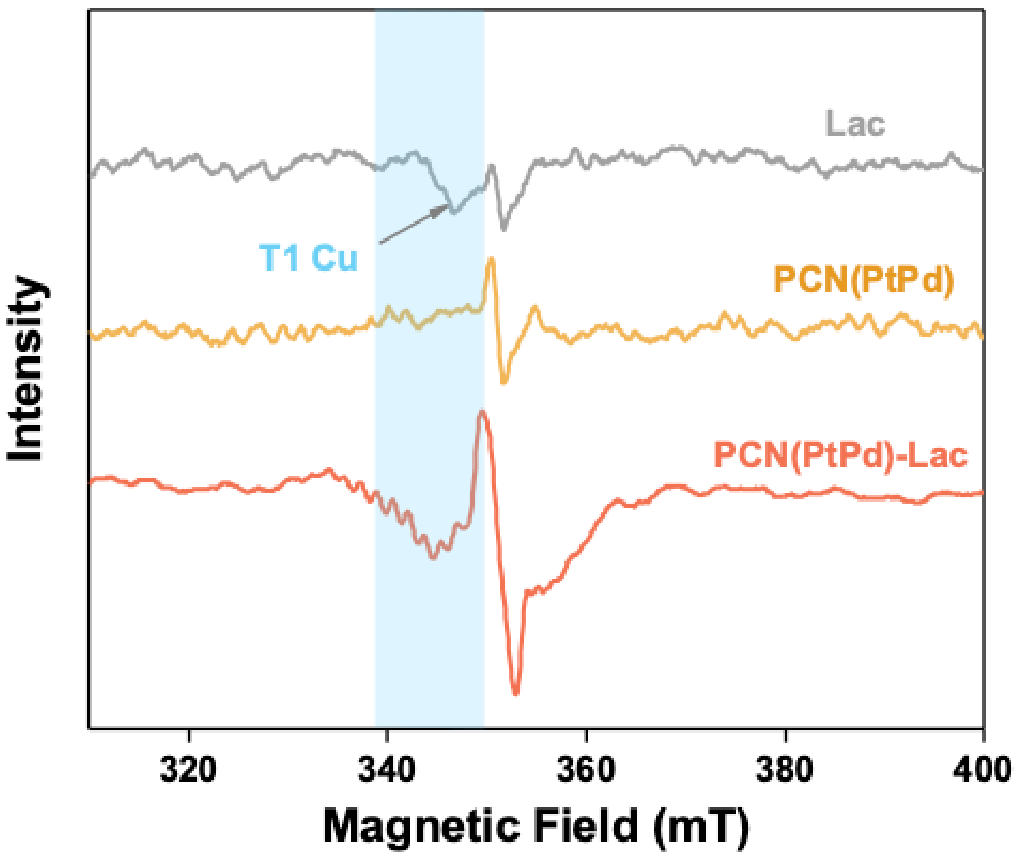

Supplementary Figure 56. ESR spectra of Lac, PCN(PtPd), and PCN(PtPd)-Lac. **e,** Scheme for the simultaneous action of reduction reaction and oxidation reaction in the laccase-PtPd hybrid active site

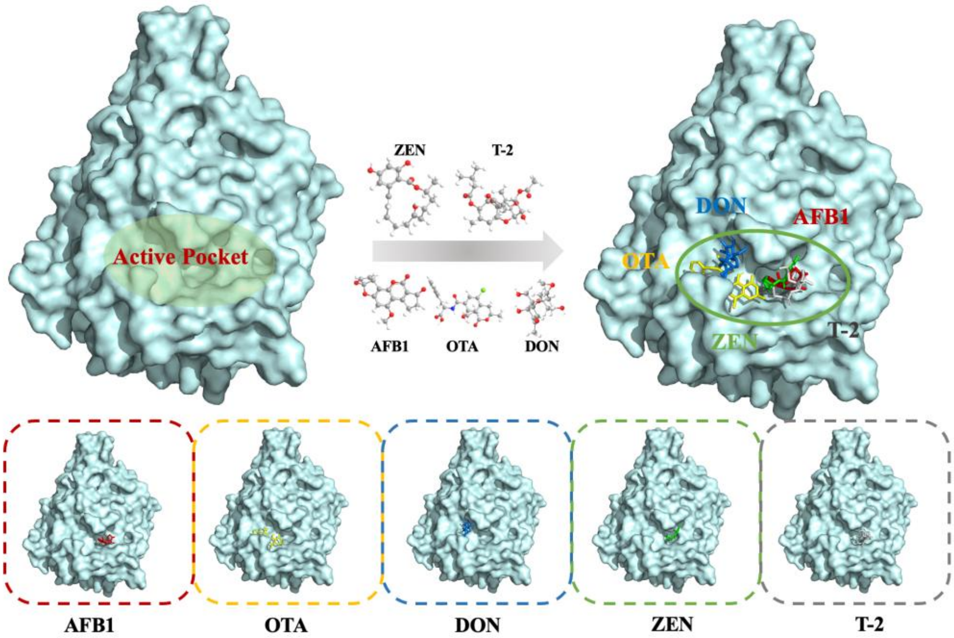

Supplementary Figure 57. Schematic representation of the binding sites between laccase and mycotoxins (AFB_1, OTA, DON, ZEN, and T-2 toxin) as demonstrated through molecular docking.

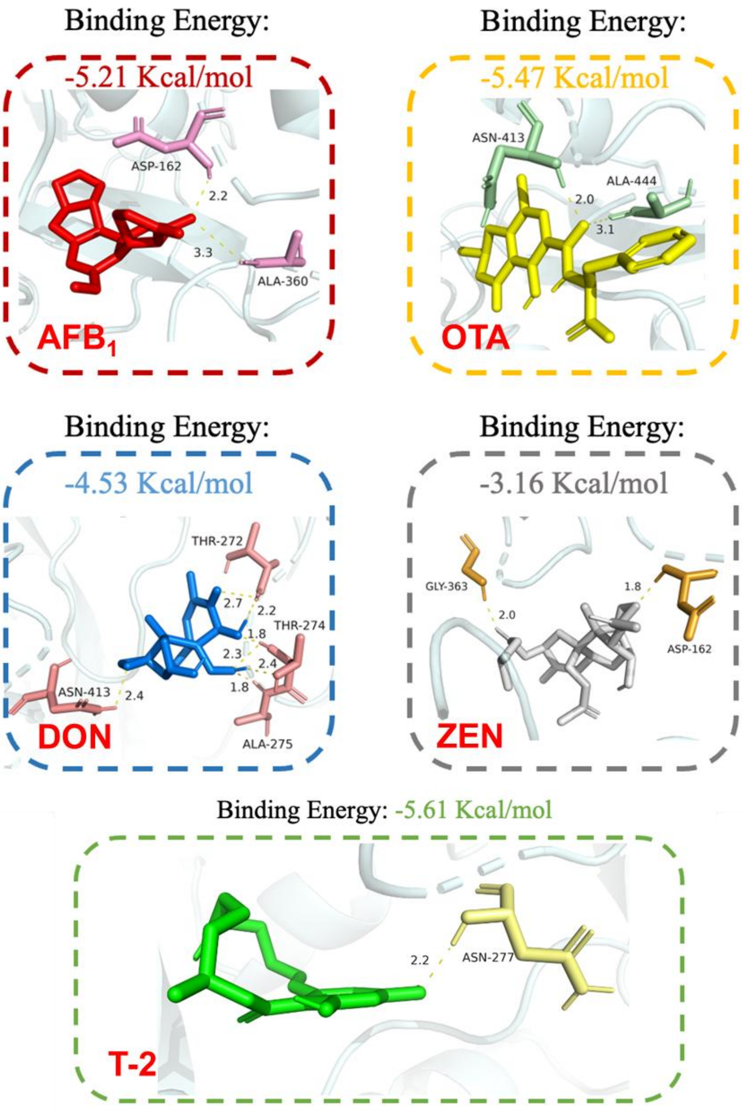

Supplementary Figure 58. Detailed schematic representation of the binding sites between laccase and mycotoxins (AFB$_1$, OTA, DON, ZEN, and T-2 toxin) as illustrated through molecular docking.

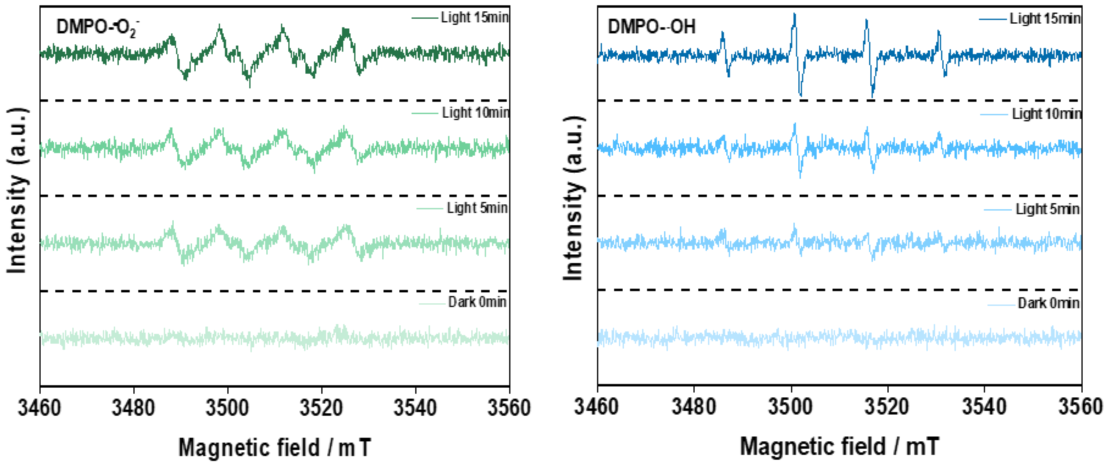

Supplementary Figure 59. ESR spectra showing the production of superoxide (O_2^-) and hydroxyl (·OH) radicals under light irradiation (Xe-lamp, 100 mW/cm^2).

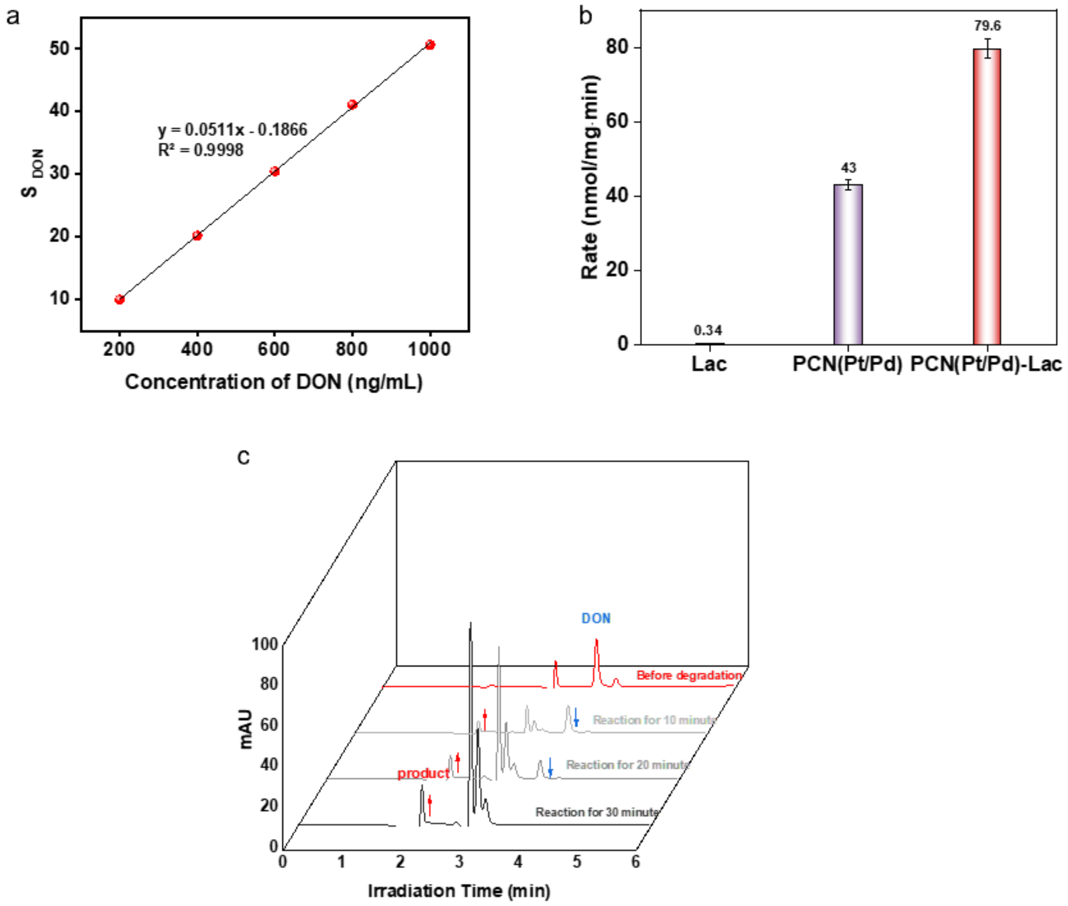

Supplementary Figure 60. Photocatalytic transformation of DON by PCN(PtPd)-Lac. (a) Calibration curve. (b) Comparison of degradation rates (nmol/mg·min) for free laccase (Lac), PCN(PtPd), and PCN(PtPd)-Lac. (c) HPLC chromatograms showing the changes in DON concentration during the reaction within 0–30 min. The decrease in the DON peak and the appearance of product peaks demonstrate the effective photocatalytic transformation of DON by PCN(PtPd)-Lac.

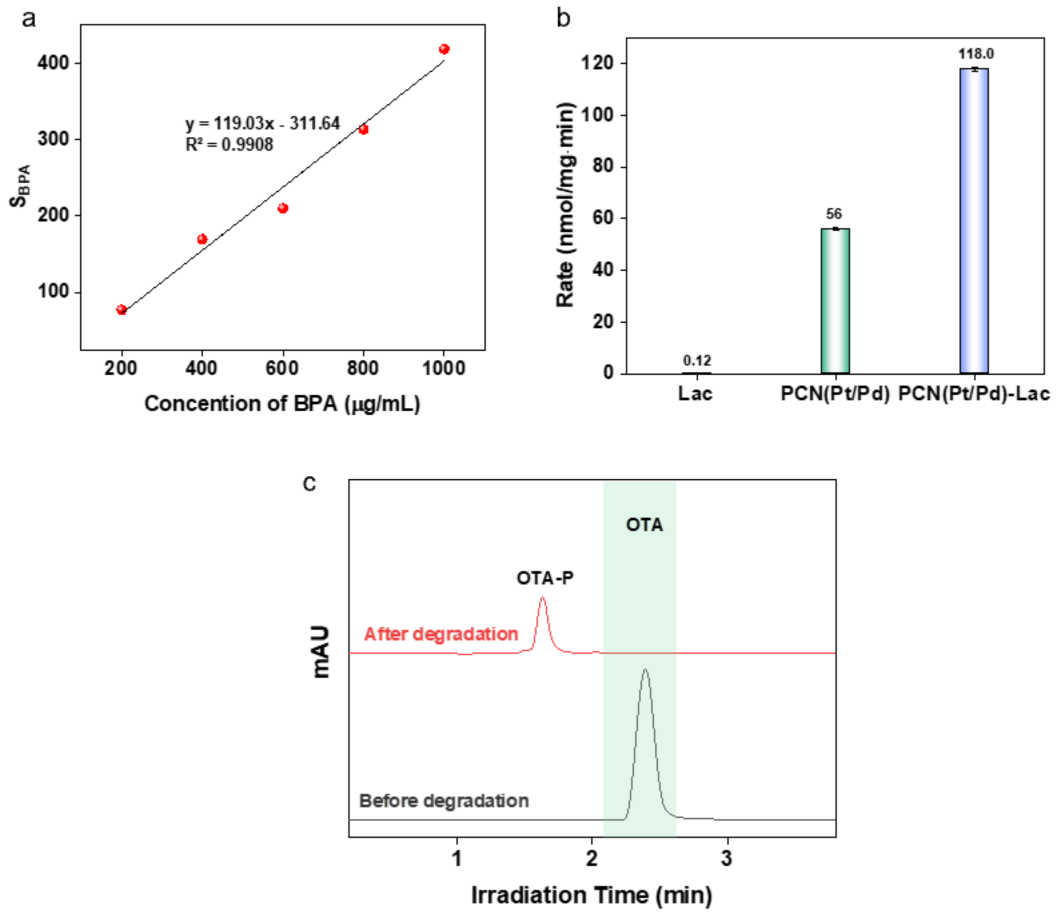

Supplementary Figure 61. Photocatalytic transformation of OTA by PCN(PtPd)-Lac. (a) Calibration curve. (b) Comparison of degradation rates (nmol/mg·min) for free laccase (Lac), PCN(PtPd), and PCN(PtPd)-Lac. (c) HPLC chromatograms showing the changes in OTA concentration during the reaction within 0–30 min. The decrease in the OTA peak and the appearance of product peaks demonstrate the effective photocatalytic transformation of OTA by PCN(PtPd)-Lac.

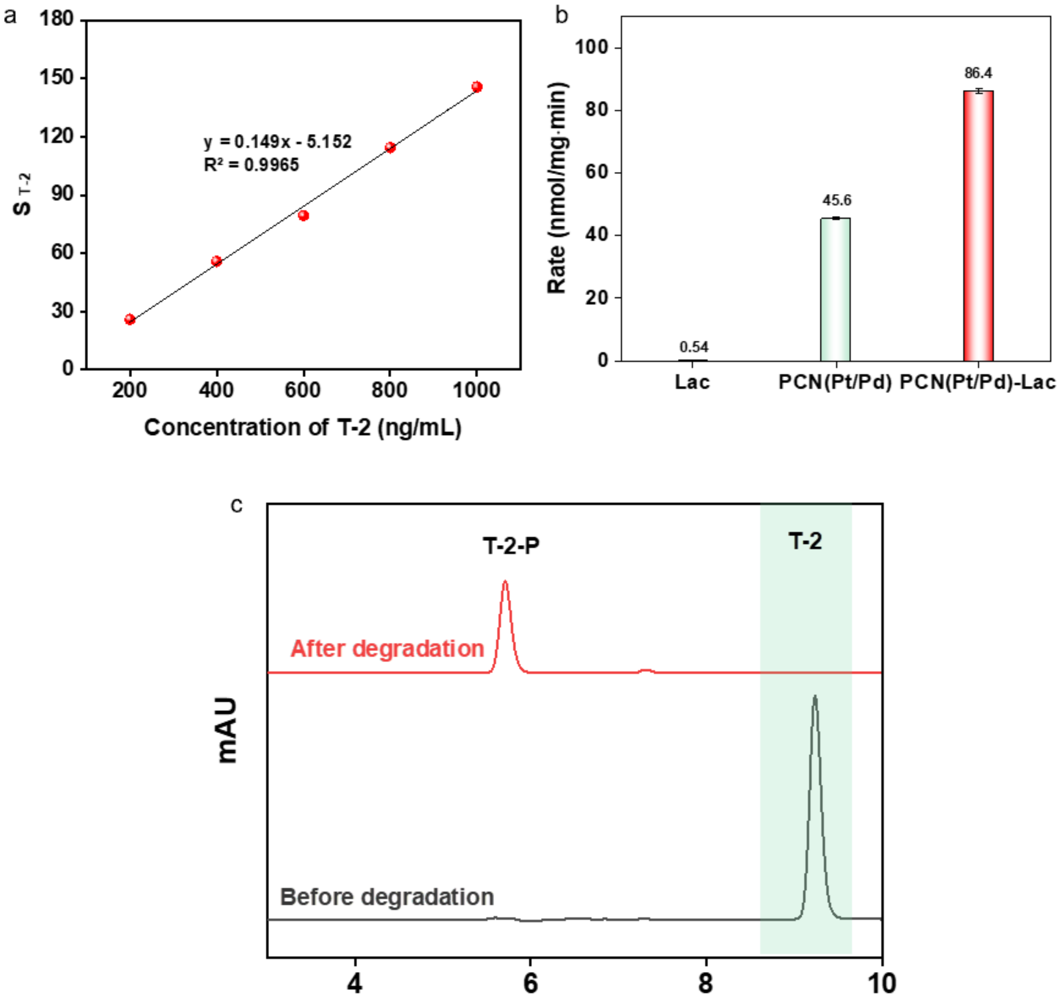

Supplementary Figure 62. Photocatalytic transformation of T-2 by PCN(PtPd)-Lac. (a) Calibration curve. (b) Comparison of degradation rates (nmol/mg·min) for free laccase (Lac), PCN(PtPd), and PCN(PtPd)-Lac. (c) HPLC chromatograms showing the changes in T-2 concentration during the reaction within 0–30 min. The decrease in the T-2 peak and the appearance of product peaks demonstrate the effective photocatalytic transformation of T-2 by PCN(PtPd)-Lac.

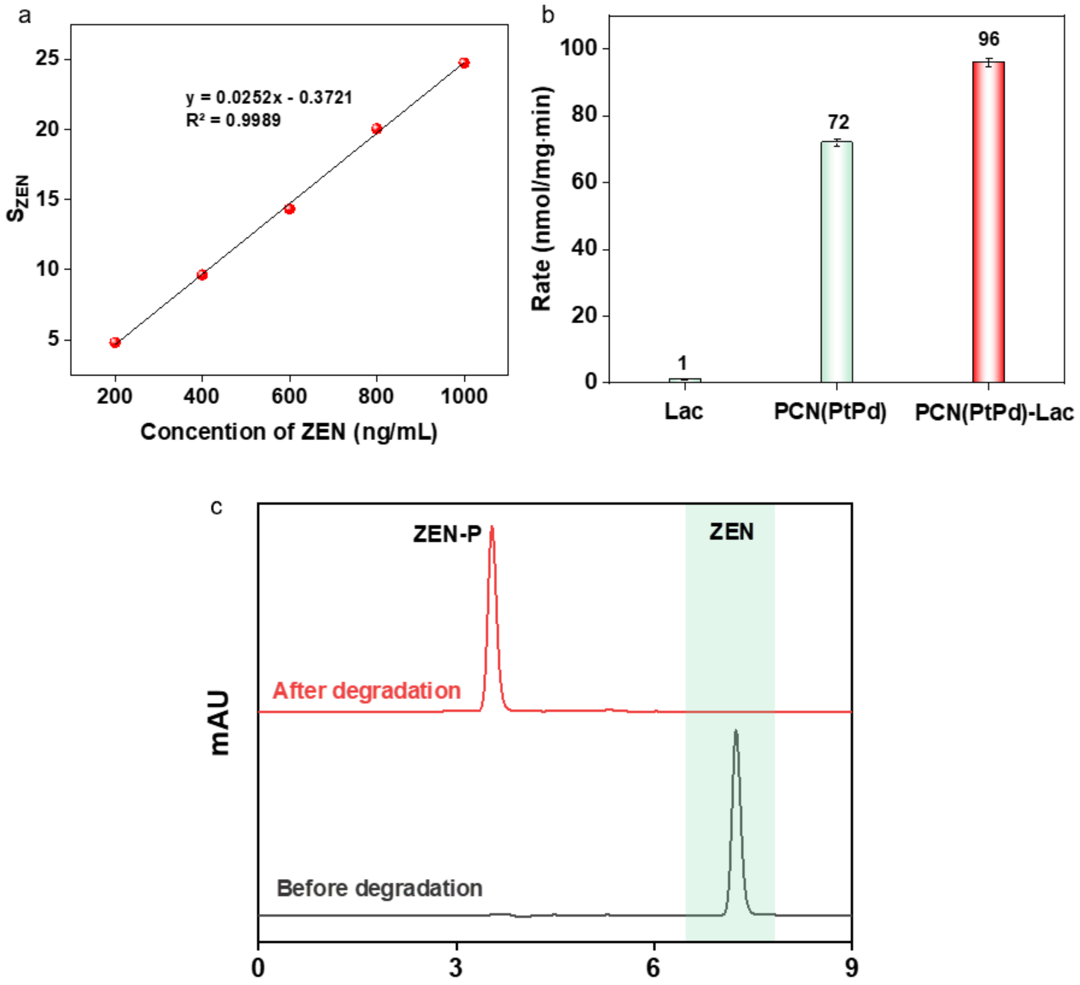

Supplementary Figure 63. Photocatalytic transformation of ZEN by PCN(PtPd)-Lac. (a) Calibration curve. (b) Comparison of degradation rates (nmol/mg·min) for free laccase (Lac), PCN(PtPd), and PCN(PtPd)-Lac. (c) HPLC chromatograms showing the changes in ZEN concentration during the reaction within 0–30 min. The decrease in the ZEN peak and the appearance of product peaks demonstrate the effective photocatalytic transformation of ZEN by PCN(PtPd)-Lac.

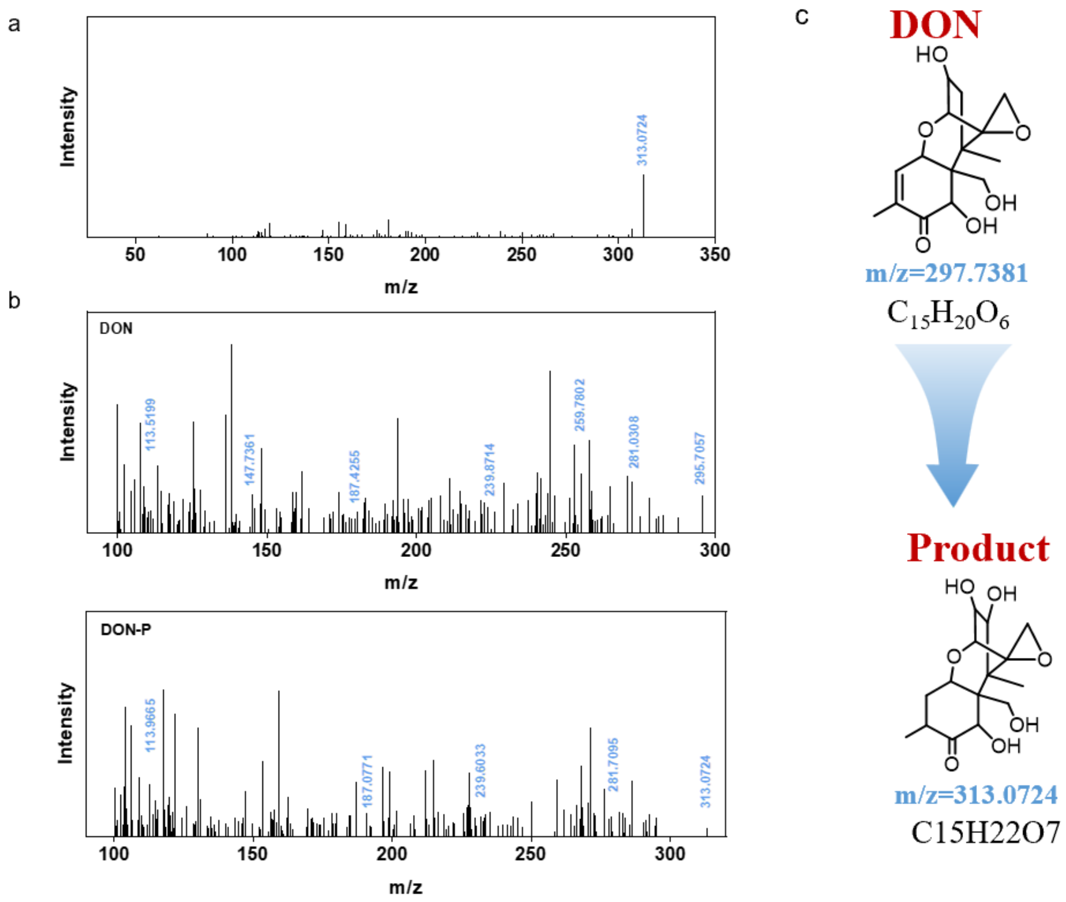

Supplementary Figure 64. (a) MS spectrum of DON transformation product. (b) MS-MS spectra of DON and transformation product. (c) Structure of DON transformation product.

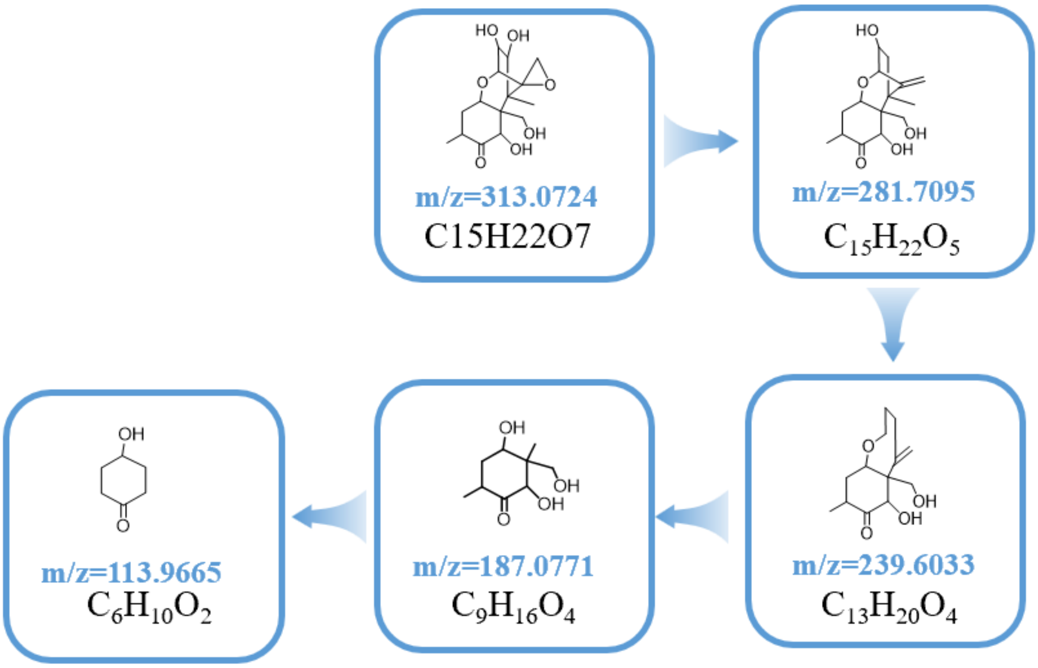

Supplementary Figure 65. Fragmentation pathway of DON transformation product in UPLC-QTOF-MS.

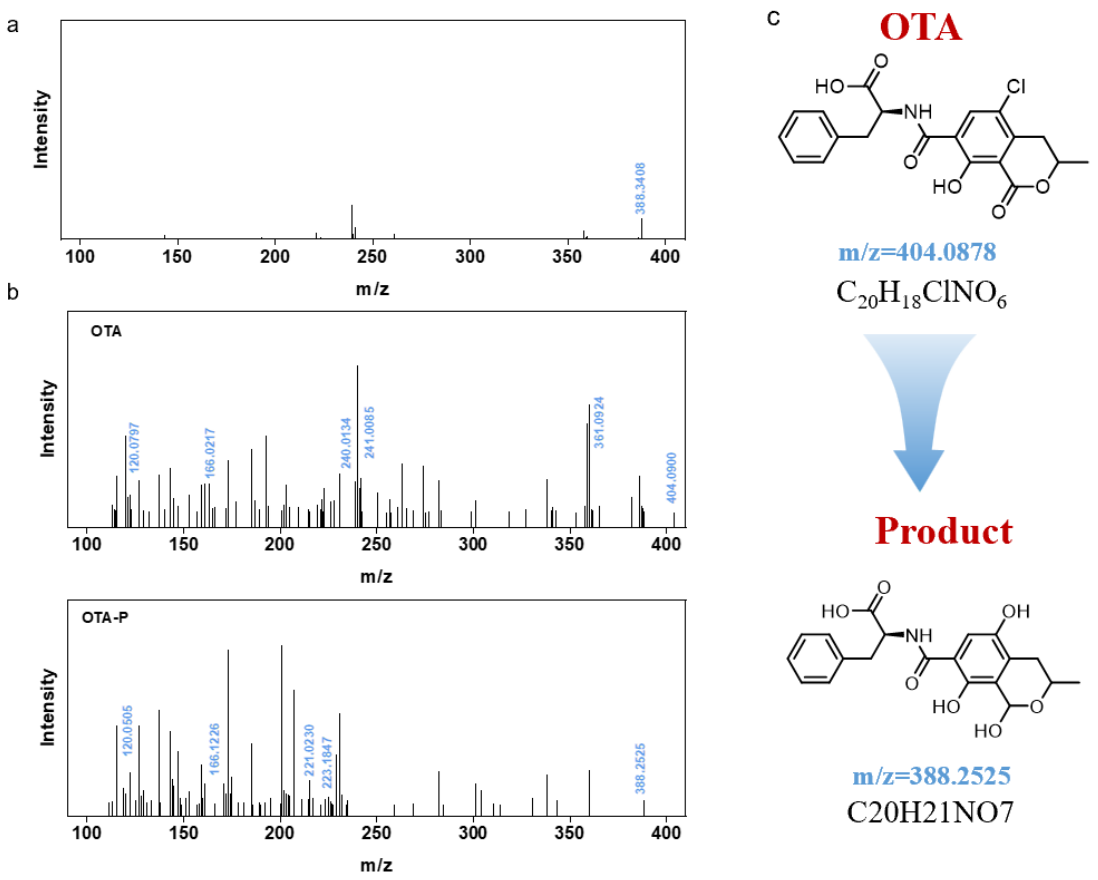

Supplementary Figure 66. (a) MS spectrum of OTA transformation product. (b) MS-MS spectra of OTA and transformation product. (c) Structure of OTA transformation product.

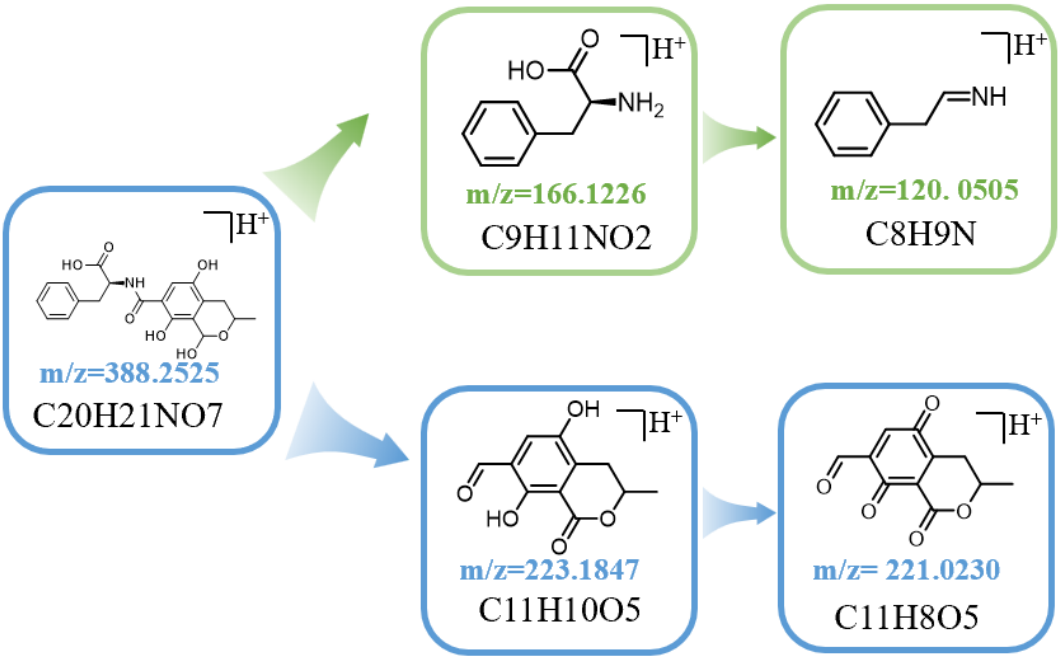

Supplementary Figure 67. Fragmentation pathway of OTA transformation product in UPLC-QTOF-MS.

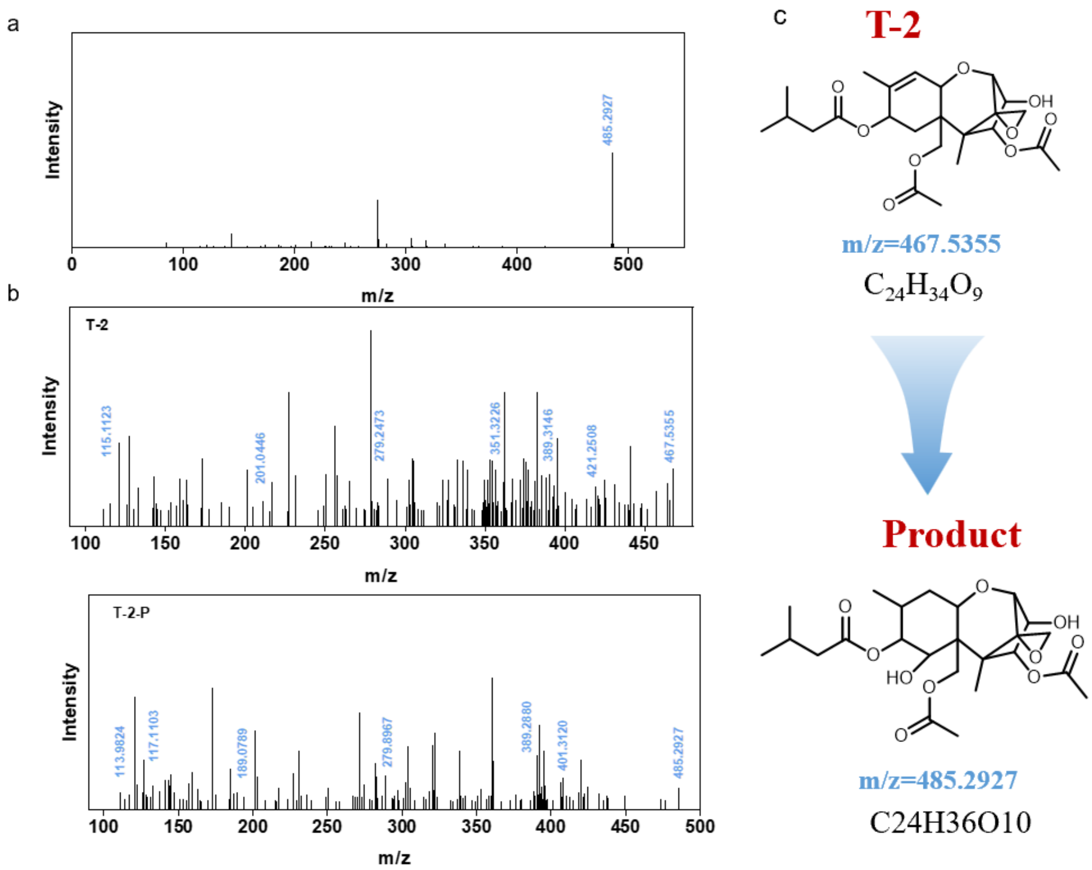

Supplementary Figure 68. (a) MS spectrum of T-2 transformation product. (b) MS-MS spectra of T-2 and transformation product. (c) Structure of T-2 transformation product.

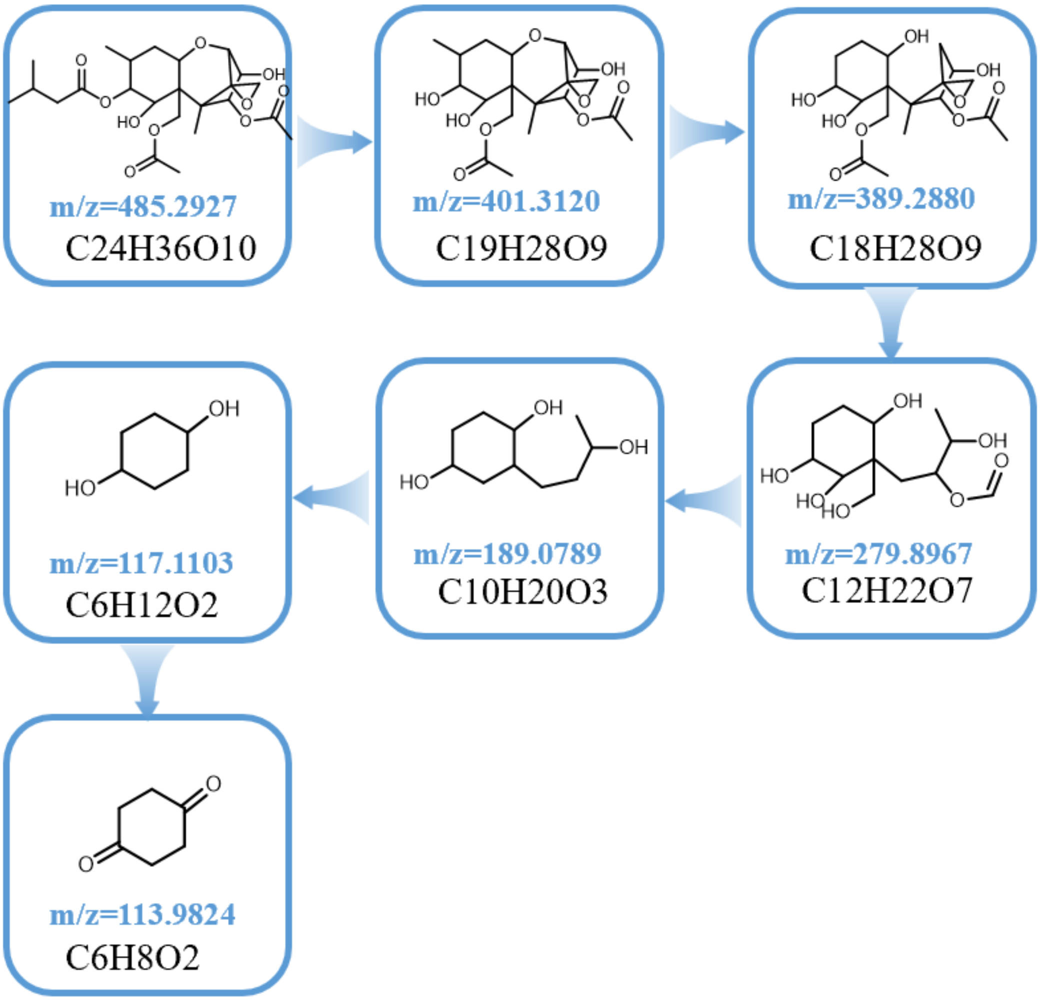

Supplementary Figure 69. Fragmentation pathway of T-2 transformation product in UPLC-QTOF-MS.

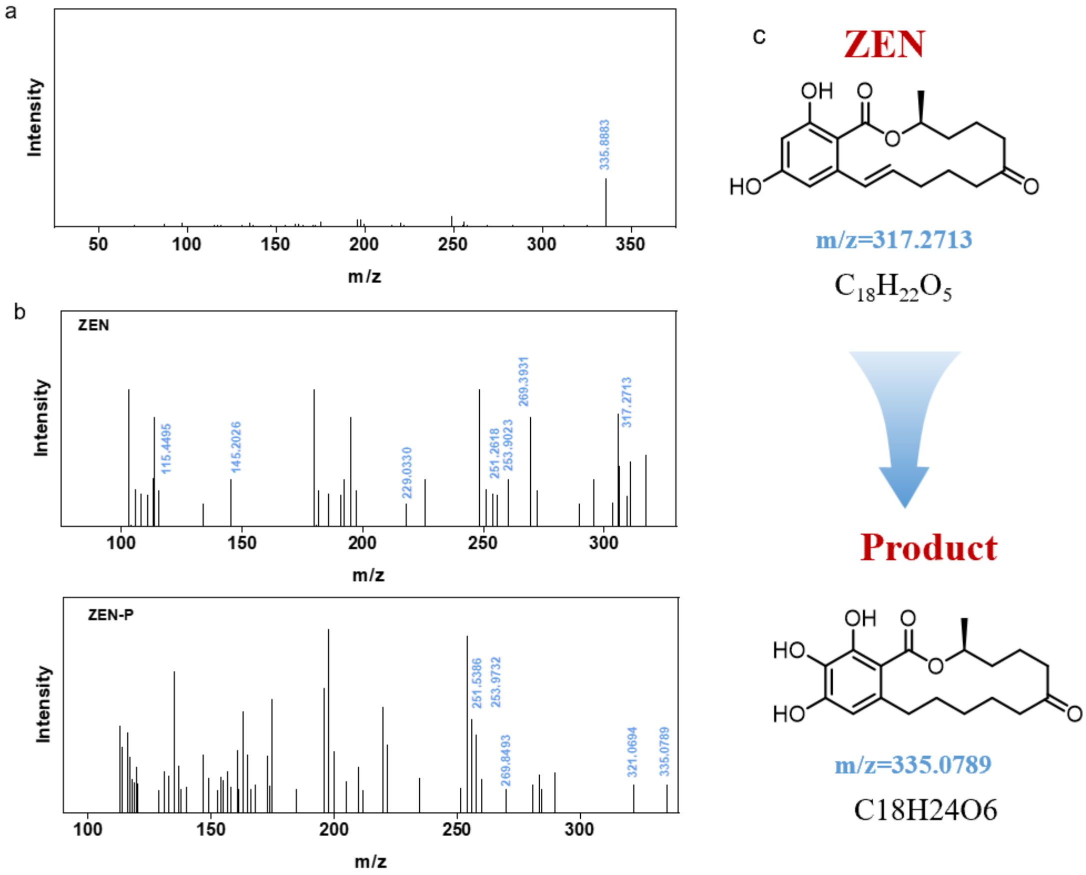

Supplementary Figure 70. (a) MS spectrum of ZEN transformation product. (b) MS-MS spectra of ZEN and transformation product. (c) Structure of ZEN transformation product.

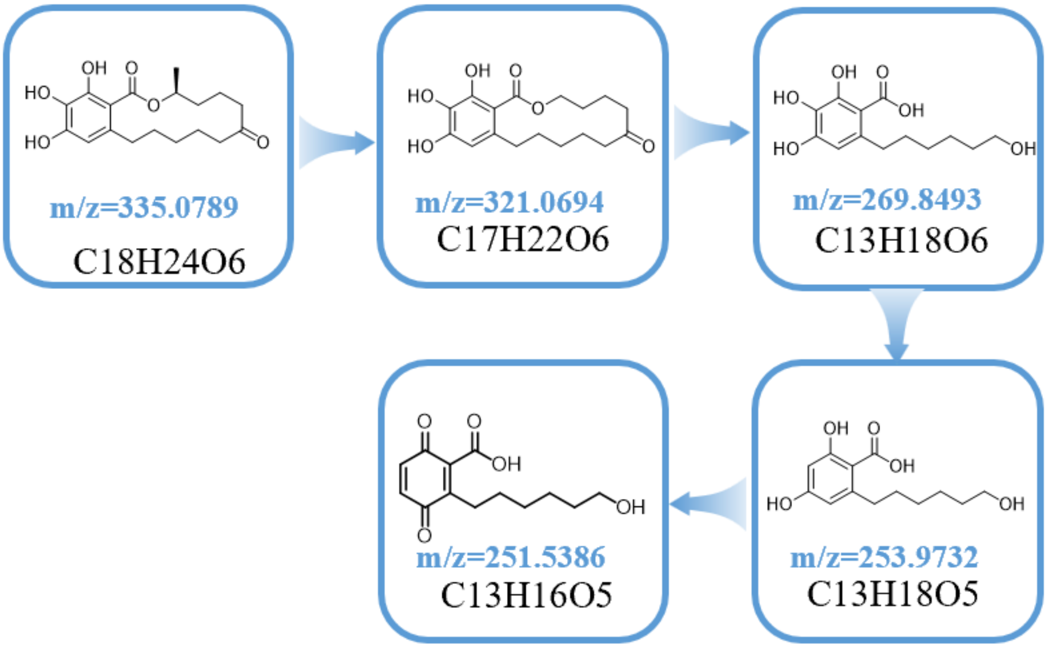

Supplementary Figure 71. Fragmentation pathway of ZEN transformation product in UPLC-QTOF-MS.

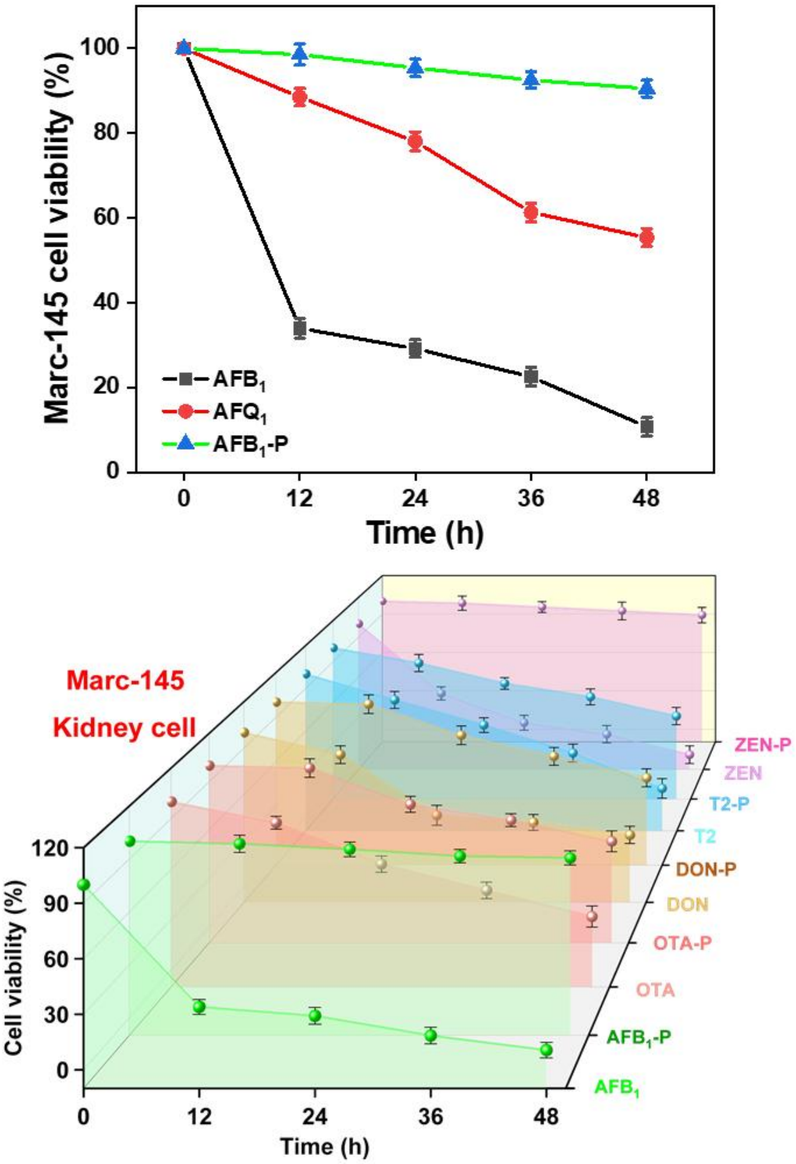

Supplementary Figure 72. (a) Cell viability assay of Marc-145 kidney cells treated with AFB$_1$, AFQ$_1$ (transformation product catalyzed by Lac+ABTS), and AFB$_1$-P at concentration of 1 mg/mL. **(b)** Cell viability assay of Marc-145 kidney cells treated with AFB$_1$, AFQ$_1$, and AFB$_1$-P at concentration of 1 mg/mL.

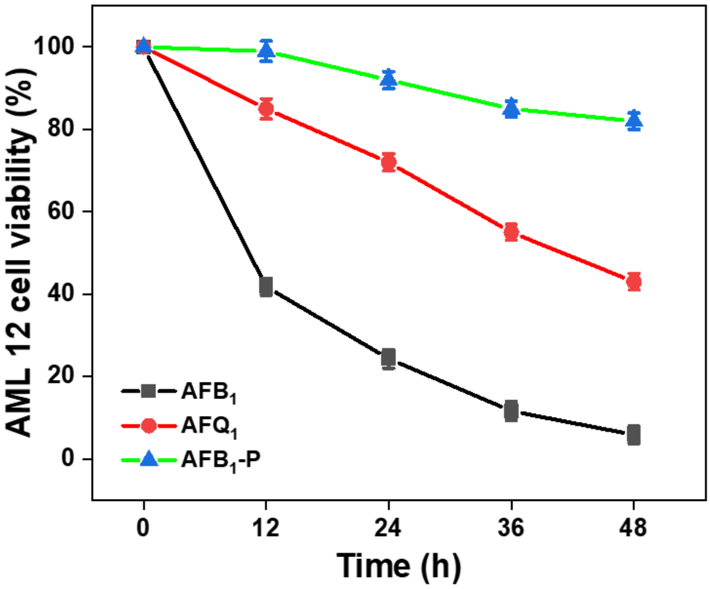

Supplementary Figure 73. Cell viability assay of AML 12 liver cells treated with AFB$_1$, AFQ$_1$ (transformation product catalyzed by Lac+ABTS), and AFB$_1$-P at concentration of 1 mg/mL.

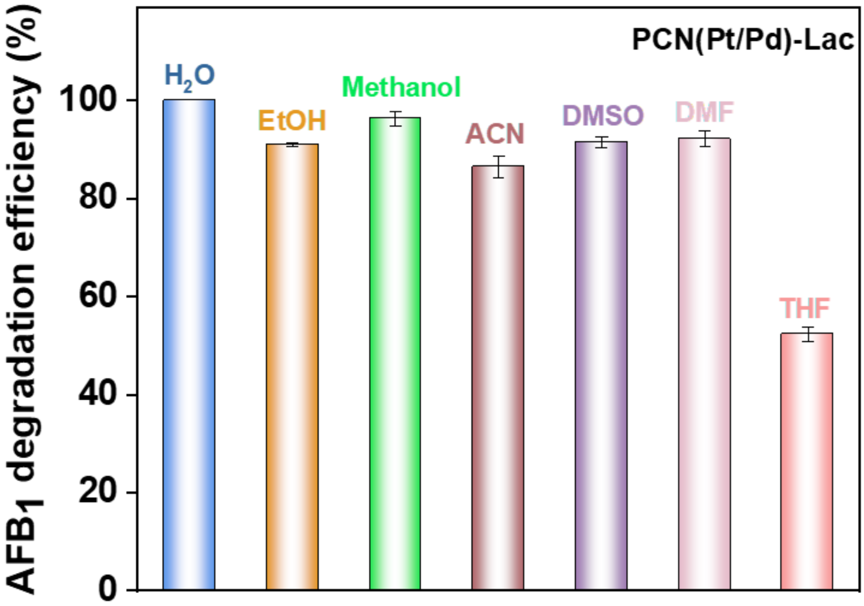

Supplementary Figure 74. The stability of PCN(PtPd)-Lac after treatment in various solvents for 30 minutes.

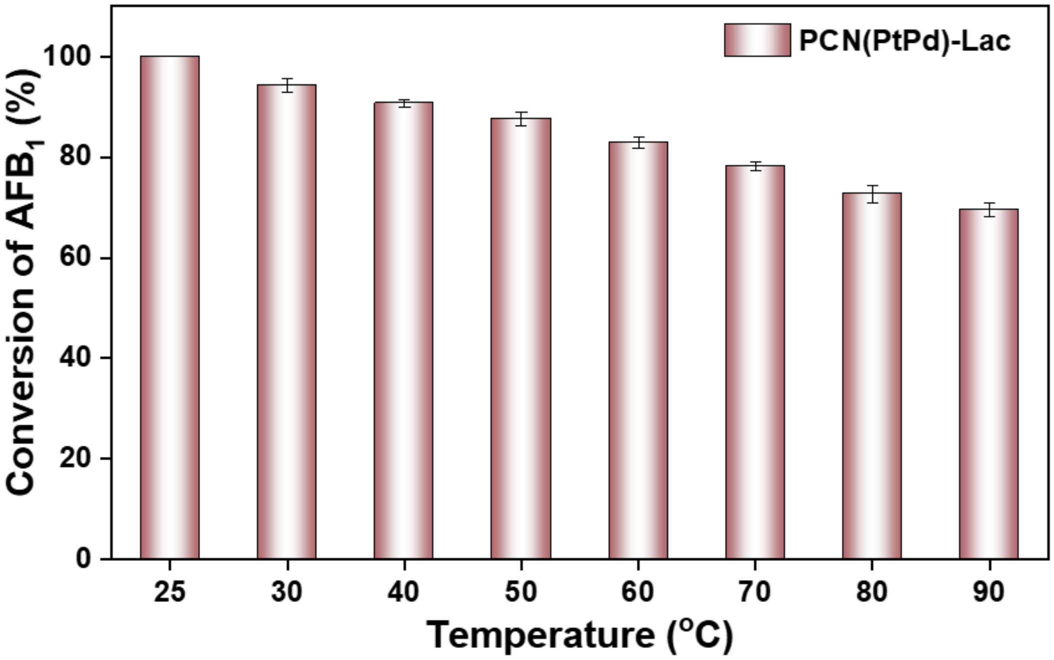

Supplementary Figure 75. AFB$_1$ degradation efficiency of PCN(PtPd)-Lac at various temperatures.

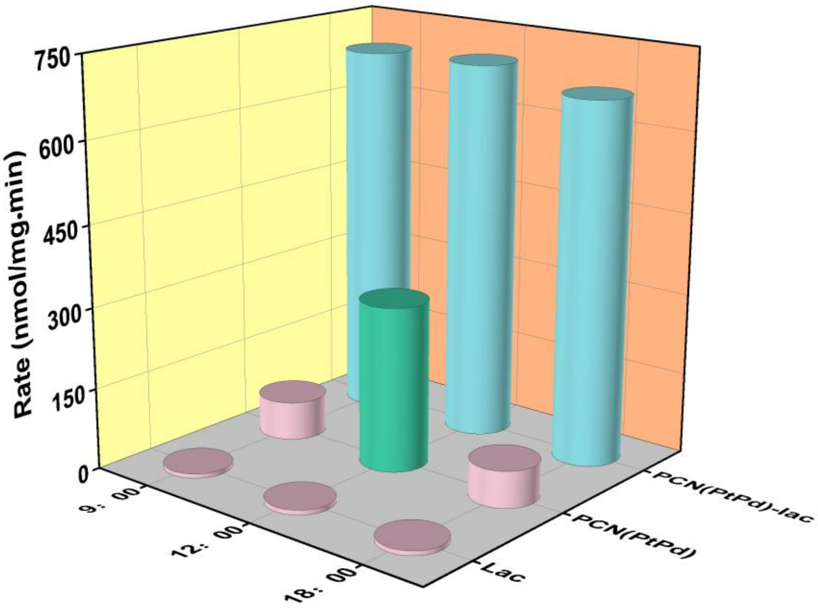

Supplementary Figure 76. Photocatalytic degradation of AFB_1 by Lac, PCN (PtPd), and PCN (PtPd)-Lac at different time points throughout September 10, 2024. The experimental data were collected in Nanchang, China, on September 10, 2024. The weather conditions throughout the day varied, influencing the measured light intensity. At 9:00 am, the weather was overcast turning partly cloudy, resulting in a relatively low light intensity of 800 lux. By 12:00 pm, partial clearing of the clouds increased sunlight exposure, leading to a peak light intensity of 2700 lux. At 6:00 pm, the weather shifted to cloudy and overcast, with light intensity decreasing to 850 lux. These variations in weather and light intensity are critical for understanding the photocatalytic degradation behaviour observed in the experiment.

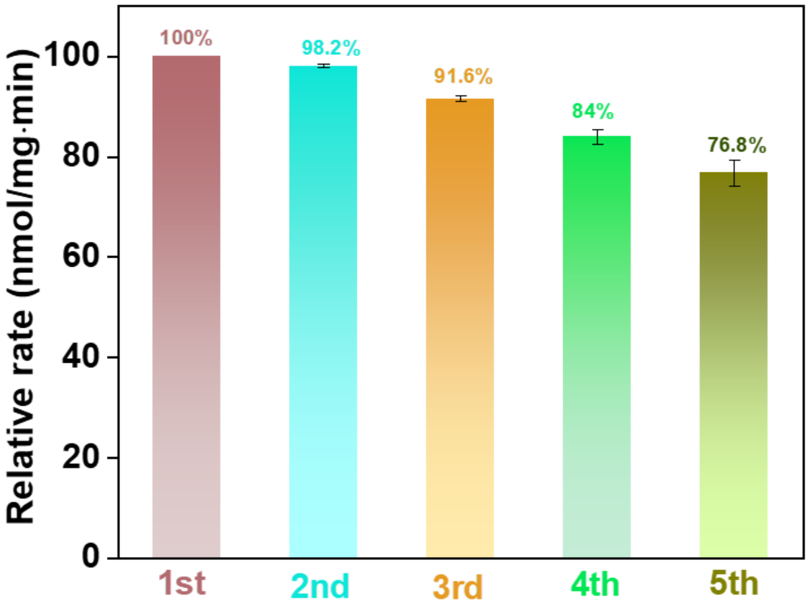

Supplementary Figure 77. Recyclability of PCN(PtPd)-Lac for AFB_1 degradation. The graph displays the relative degradation rates (nmol/mg·min) of PCN(PtPd)-Lac over five consecutive cycles. The degradation efficiency remains high, with a gradual decrease observed across cycles, retaining 76.8% of the initial activity after the fifth cycle. This result demonstrates the catalyst's recyclability and stability for repeated AFB_1 degradation.

Supplementary Tables

Supplementary Table 1. ICP results for mass loading in single-atom implanted PCN(PtPd) andPCN(PtPd)-Lac.

	Zr wt%	**Pt wt%**	**Pd wt%**
PCN(Pt)	-	5.4%	-
PCN(Pd)	-	-	7.1%
PCN(PtPd)	12%	3.1%	2.7%
PCN(PtPd)-Lac	8%	1.3%	0.5%

Supplementary Table 2. Structural parameters of PCN-Pt/Pd, PtO_2 and Pt foil extracted from the EXAFS fitting.

Sample	**Shell**	**CN**	**R (Å)**	**σ^2 (Å^2)**
PCN-Pt/Pd	Pt-N	2.9	2.18	0.0145
	Pt-Cl	1.4	2.31	0.0017
PtO_2	Pt-O	4.0	2.02	0.0018
Pt foil	Pt-Pt	12	2.77	0.0046

Note: The analysis was processed by software Artemis, corresponding to the EXAFS spectra. CN, coordination number; R, bonding distance; σ^2, Debye-Waller factor; ΔE_0, shift in absorption edge energy.

Supplementary Table 3. Structural parameters of PCN-Pt/Pd, $Pd(OAc)_2$ and Pd foil extracted from the EXAFS fitting.

Sample	**Shell**	**CN**	**R (Å)**	**σ^2 (Å^2)**
PCN-Pt/Pd	Pd-N	4.0	2.09	0.0126
	Pd-O	1.9	2.12	0.0014
$Pd(OAc)_2$	Pd-O	4.0	2.01	0.0037
Pd foil	Pd-Pd	12	2.74	0.0056

Note: The analysis was processed by software Artemis, corresponding to the EXAFS spectra. CN, coordination number; R, bonding distance; σ^2, Debye-Waller factor; ΔE_0, shift in absorption edge energy.

Supplementary Table 4. Thermogravimetric analysis (TGA) of Lac, PCN(PtPd), and PCN(PtPd)-Lac.

	Weight at 30 ℃	**Weight at 800 ℃**	**Weight loss from 30 ℃ to 800 ℃**
Lac	100%	46.67%	53.33%
PCN(PtPd)	100%	61.98%	38.02%
PCN(PtPd)-Lac	100%	58.23%	41.77%

For PCN(PtPd)-Lac, we set the Lac weight percentage to X, and then the weight percentage of PCN(PtPd) is 1-X. Therefore, X was calculated as follows:

$$X \times 53.33\% + (1-X) \times 38.02\% = 41.77\%$$

$$X = 24.49\%$$

Supplementary Reference

[1] Li, X., et al. Electron counting and beam-induced motion correction enable near-atomic-resolution single-particle cryo-EM. Nat. Methods 10, 584 (2013).

[2] Rohou, A. & Grigorieff, N. CTFFIND4: Fast and accurate defocus estimation from electron micrographs. J. Struct. Biol. 192, 216-221 (2015).

[3] Kremer, J.R., Mastronarde, D.N. & McIntosh, J.R. Computer Visualization of Three -Dimensional Image Data Using IMOD. J. Struct. Biol. 116, 71-76 (1996).

[4] Pettersen, E.F., et al. UCSF Chimera-A visualization system for exploratory research and analysis. J. Comput. Chem. 25, 1605-1612 (2004).